



Concurrent effects of the shear-lag and warping torsion on the performance of non-rectangular RC shear walls

Mohammad Tabiee¹ · Hatf Abdoos¹ · Alireza Khaloo¹

Received: 22 August 2022 / Revised: 18 March 2023 / Accepted: 4 April 2023 / Published online: 7 May 2023
© Wrocław University of Science and Technology 2023

Abstract

This paper aimed at analytically investigating the simultaneous effects of the shear-lag and warping torsion on the performance of non-rectangular reinforced concrete (RC) shear walls. Under the concurrent action of shear and axial loadings, the induced warping deformation due to the shear-lag as well as the warping torsion has been accounted for in the elastic region. On the strength of the minimum potential energy principle, a general formulation has been derived for the stress distribution of non-rectangular RC shear walls. By introducing the appropriate geometrical assumptions, the established formulations have then been re-written for conventional T-, U-, and L-shapes RC shear walls. The veracity of the results is ascertained through a comparative study employing finite element simulations for a U-shaped wall, and good agreement has been achieved to an extent that the proposed analytical formulation is capable to, respectively, predict the axial deformation and stress distribution with an accuracy of 95 and 90%. Also, the findings for the U-shaped wall indicate that the shear-lag can significantly affect the axial stress distribution and cracking load, and neglecting the influence of this phenomenon can lead to an inaccurate and a non-conservative design. Moreover, the contribution of the shear-lag and warping torsion has separately been highlighted for the U-shaped RC wall considered in this study.

Keywords Shear-lag · Non-rectangular RC shear wall · Analytical study · FE analysis · Minimum potential energy (MPE) · Warping torsion

List of symbols

α_x, α_y	Dimensionless coefficients in warping deformation resulting from the shear-lag in x - and y -directions	ϵ_t	Strain corresponding to the ultimate tensile strength of concrete
β_x, β_y	Constants in warping deformation resulting from the shear-lag in x - and y -directions	ϵ_{tu}	Ultimate tensile strain of concrete
γ_t	Product of α_x and b_t	$\lambda_b, \lambda_c, \lambda_t$	Constants corresponding to the shear-lag effects in x - and y -directions, and torsional moment
ϵ_{50}	Strain corresponding to the stress of $0.50f'_c$ after attaining the maximum compressive strength of concrete	μ_s	The ratio of the maximum tensile stress with shear-lag and warping torsion to the maximum tensile stress of the Bernoulli–Euler assumption
ϵ_{sh}	Strain at the onset of hardening stage	$\mu_{sb}, \mu_{sc}, \mu_{sd}$	Contribution of the shear-lag in x - and y -directions, and warping torsion to the additional tensile stress
ϵ_{su}	Strain corresponding to the ultimate strength of steel reinforcement	ν	Poisson's ratio of concrete
ϵ_{sy}	Strain corresponding to the yield stress of steel reinforcement	Π	Total potential energy function
		Π_b, Π_c	Total potential energy function corresponding to the lateral loads in x - and y -directions
		σ	Axial stress distribution function of RC shear wall

✉ Alireza Khaloo
khaloo@sharif.edu

¹ Department of Civil Engineering, Sharif University of Technology, Tehran, Iran

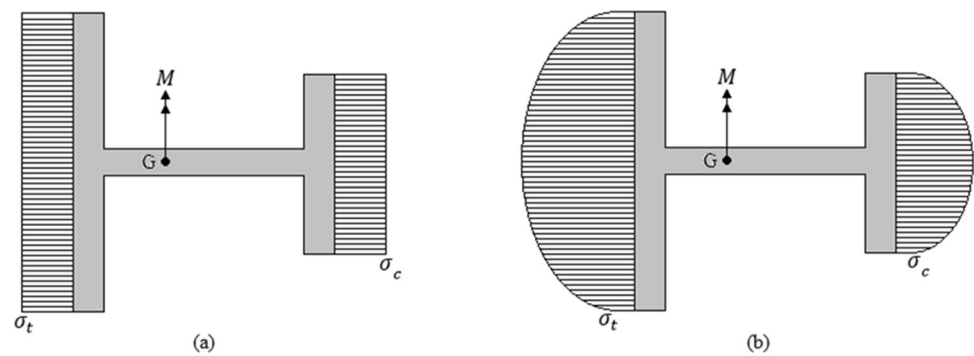
$\sigma_a, \sigma_b, \sigma_c, \sigma_d$	Axial stress distribution function under the axial load, lateral load in x - and y -directions, and torsional moment	U_{fb}, U_{ft}, U_w	Strain energy functions corresponding to the bottom flange, top flange, and web of the section
$\bar{\sigma}$	Stress distribution function with the Bernoulli–Euler assumption	u	Axial deformation function of RC shear wall
$\bar{\sigma}_b, \bar{\sigma}_c$	Stress distribution function with the Bernoulli–Euler assumption in x - and y -directions	u_a, u_b, u_c, u_d	Axial deformation function induced by axial load, lateral load in x - and y -directions, and torsional moment
τ	Shear stress distribution function of RC shear wall	u_{wb}, u_{wc}	Shear-lag constants in x - and y -directions
ϕ	Torsional moment-induced rotation angle	V_L	Potential energy due to the external loads
ψ	Warping function	V_{Lb}, V_{Lc}	Potential energy due to the external loadings in x - and y -directions
A	Cross-sectional area of the wall	V_x, V_y	Lateral loadings in x - and y -directions
B	Bi-moment	$V_{x(max)}, V_{y(max)}$	Maximum calculated lateral load in x - and y -directions before cracking, based on the Bernoulli–Euler assumption
$b_{fbL}, b_{fbR}, b_{ftL}, b_{ftR}$	Widths of the left-side bottom flange, right-side bottom flange, left-side top flange, and right-side top flange	$V'_{x(max)}, V'_{y(max)}$	Maximum calculated lateral load in x - and y -directions before cracking due to the shear-lag and warping torsion
b_t	Horizontal component of the centroid coordinate of the wall in (\hat{x}, \hat{y}) coordinate	w_x, w_y	Lateral deformation of the wall in x - and y -directions before cracking, based on the Bernoulli–Euler assumption
C_w	Warping constant	(x_c, y_c)	Shear center coordinate of the section
d_c	Confined length of the section	(x_G, y_G)	Centroid coordinate of the section
E	Equivalent modulus of elasticity of the wall		
e_c	Clear cover		
e_x, e_y	Eccentricity of the lateral loads in y - and x -directions from the shear center		
f_u	Ultimate stress of steel reinforcement		
f_y	Yield stress of steel reinforcement		
f'_c	Compressive strength of concrete		
f'_t	Tensile strength of concrete		
G	Shear modulus of the wall structure		
H	Height of the wall		
h	Shear wall section height		
h_b, h_t	Centroid distance from the center of the bottom and top flanges		
$I_{eb}, I_{wb}, I_{ec}, I_{wc}$	Shear-lag constants in x - and y -directions		
I_x, I_y	Moment of inertia about x - and y -axes		
\bar{I}_x, \bar{I}_y	Moment of inertia about \bar{x} - and \bar{y} -axes		
J	Torsional moment of inertia		
N	Applied axial loading		
$M_{\bar{x}}, M_{\bar{y}}$	Moment of the section about \bar{x} - and \bar{y} -axes		
q	Axial stress of RC shear wall		
s_x, s_y	Shear-lag induced additional lateral deformation in x - and y -directions		
t_{fb}, t_{ft}, t_w	Thickness of the bottom flange, top flange, and web		

1 Introduction

Non-rectangular reinforced concrete (RC) shear walls have increasingly been utilized in recent years due to the architectural limitations and structural efficiency reasons. Among the conventional non-rectangular RC shear walls are the I-, T-, U-, L-, C- and Z-shaped configurations.

The Bernoulli–Euler assumption, i.e., the wall's cross-section remains plane and perpendicular to the neutral axis after bending, is the case for non-rectangular RC shear walls only when no shear load is applied to the section or the shear stiffness of the wall is infinite [1]. In fact, the sections of flanged walls may experience shear deformations due to the transfer of shear flow from the web to the flange. Therefore, the axial stress and strain in the vicinity of the web-flange connection are larger in comparison to other areas (see Fig. 1). This phenomenon is known as the shear-lag [1, 2], and its inevitable effects in the analysis and design of different structural elements have been addressed in the previous studies [3–9].

Fig. 1 Stress distribution: **a** without shear-lag, and **b** with shear-lag effect



In comparison with the Bernoulli–Euler assumption, considering the shear-lag increases the maximum induced axial stress of the section at the web–flange conjunctions, which can attenuate the flexural capacity of the wall. Indeed, negligence of the shear-lag effects in the analysis of non-rectangular RC shear walls can lead to a non-conservative design [1, 2]. With this in mind, many studies attempted to evaluate the effects of the shear-lag on non-rectangular RC shear walls. However, in recent years, there are quite a few papers employing the experimental [10–16] or numerical [2, 17–19] approaches to evaluate the shear-lag effects, and limited investigations have been devoted to analytically address the shear-lag phenomenon on the response of non-rectangular RC shear walls, of which a brief survey is provided herein.

As the initial contribution to the shear-lag effect, Reissner [20] analytically investigated the influence of the shear-lag on box beams. A second-order function was adopted to account for the shear-lag induced axial deformations, and then, based on the minimum potential energy (MPE) principle, four basic examples were analyzed. The results indicated the significant contribution of the shear-lag to both the deflection and stress distribution of a box beam.

Implementing the finite element approach, Kwan [1] investigated the shear-lag phenomena on shear/core walls. By fine meshing the wall structures and conducting parametric study, some formulation has been established to calculate the axial stress and strain distribution at the core sections. In the Kwan's proposed method, the core-shaped structure was divided into two U-shaped congruent walls to decrease the computation cost and simulation time by analyzing each section independently. It is to mention that the warping torsion was not included in the finite element (FE) process due to the fact that the loading was applied parallel to each web of the U-shaped section.

By employing fundamental elasticity theory equations and Fourier series, Song and Scordelis [21] proposed an effective analytical approach to describe the shear-lag effect on the elastic behavior of T-section, I-section, and box beams. Haji-Kazemi and Company [22] incorporated the shear-lag into the Airy stress functions, and then, based on

the power series, the equilibrium and compatibility equations of a high-rise tube structure have been established.

Due to the shear-lag effects, and in turn, the complexities do exist in the behavior of non-rectangular flanged RC shear walls; conventional design codes introduce an effective flange width ratio to further simplify the calculation process of flanged sections [23–27]. According to the recommendations of these codes, the shear-lag effects are ignored during the design and analysis process, and instead, the proposed effective width of flange is only considered. Furthermore, a wealth of studies [18, 28–31] reported that the effective width ratios proposed by the conventional design codes are, in many cases, inaccurate in assessing the shear-lag phenomenon. It is worthy of mention that, the main focus of all the mentioned studies are mainly on the shear-lag effects, and the influences of the warping torsion have essentially been ignored in the effective width estimation of non-rectangular flanged sections.

Shi and Wang [32] approximated the shear-lag induced warping deformation as a third-order function in order to derive an analytical formulation for the stress distribution and effective flange width of T-shaped walls in the elastic range, and the veracity of the approximation has then been examined through a finite element analysis. Moreover, Liu et al. [33] highlighted the strong influence of the shear-lag on the axial stress distribution as well as the deformation of T-shaped RC shear walls.

In addition, Ni and Cao [34] developed a general formulation for the stress distribution of I-shaped Beams and shear walls with two asymmetric flanges, in which the contribution of the shear-lag induced warping deformation has been applied through a second-order function. In a comprehensive study, Lu and Li [35] proposed equations for the effective flange width calculation of T-section RC shear walls by considering the shear-lag phenomenon in this section. They calculated the effective section width in the elastic range employing the energy equations, and thereafter using FE modeling, a parametric study was carried out in the non-linear region in order to estimate the effective flange width. Zhang et al. [18] adopted a theoretical solution to explore the shear-lag influence as well as the strain nonlinearity

introduced in RC shear walls with different kind of flanged sections. Moreover, they proposed a semi-empirical equation to assess the lateral cyclic loading effect on the unevenness of the compressive strains induced in the wall flanges. Furthermore, in recently published papers by the authors [36, 37], the shear-lag effects have been highlighted on the response of L-shaped RC shear walls, and then through the EPR algorithm, an applicable formulation was proposed for the effective width estimation of L-shaped RC shear walls.

A brief review of the literature clearly indicates that the analytical investigations are mainly focused on the specific cross-sections which are essentially symmetric and cannot be extended to all flanged sections. This is while particular attention should be given to asymmetric non-rectangular flanged sections which may find application depending on the structural and aesthetic considerations.

It should be noted that torsional moments are also introduced into the RC shear walls with asymmetric sections due to the shear eccentricity. In that regard, in addition to the torsional deflections, warping deformation does occur in the section due to the shear-lag which can modify the axial displacement, and in turn, the axial stress distribution of the wall. Through the analytical and numerical approaches, a torsional analysis has also been performed in which the effects of warping torsion has separately been evaluated for a wide range of sections [38–41].

Nevertheless, to the best knowledge of the authors, the effects of warping torsion as well as shear-lag on non-rectangular RC shear walls have rarely been simultaneously studied in the literature. Hence, the current study offers a general formulation wherein the shear-lag together with the warping torsion are introduced into the axial displacement and stress distribution of non-rectangular RC shear walls. Then, employing the FE analysis, the reliability and veracity of the proposed formulation will be ascertained in the upcoming sections.

2 Stress distribution and deformation functions

2.1 Basic assumptions

As previously mentioned, the present study deals with the analysis of flanged RC shear walls with a general asymmetric cross-section under the lateral and axial loadings. The geometrical characteristics of an arbitrary wall section is demonstrated in Fig. 2. In order to fill the gap addressed in the literature [42], the current study presents the axial stress distribution and deformation functions of non-rectangular RC shear walls due to the both components of the in-plane lateral loading (V_x , V_y).

As shown in Fig. 2c, the points G and C , respectively, denote the centroid and shear center of the section. Also, e_y and e_x are the eccentricities of the lateral loadings V_x and V_y in the positive directions, respectively, and the axial load, N , has been applied to the centroid of the section. In order to simplify modeling of the section, the confined length, d_c , and cover concrete thickness, e_c , are assumed to be constant across the section.

The minimum potential energy (MPE) principle has been employed to find the stress distribution of the section. In that regard, the following assumptions will be introduced into the problem formulation:

- A linear behavior is assumed for both steel reinforcements and concrete materials.
- The superposition principle is applied due to the linearity of the materials.
- A second-order polynomial function has been adopted to approximate the shear-lag induced axial deformation [43].

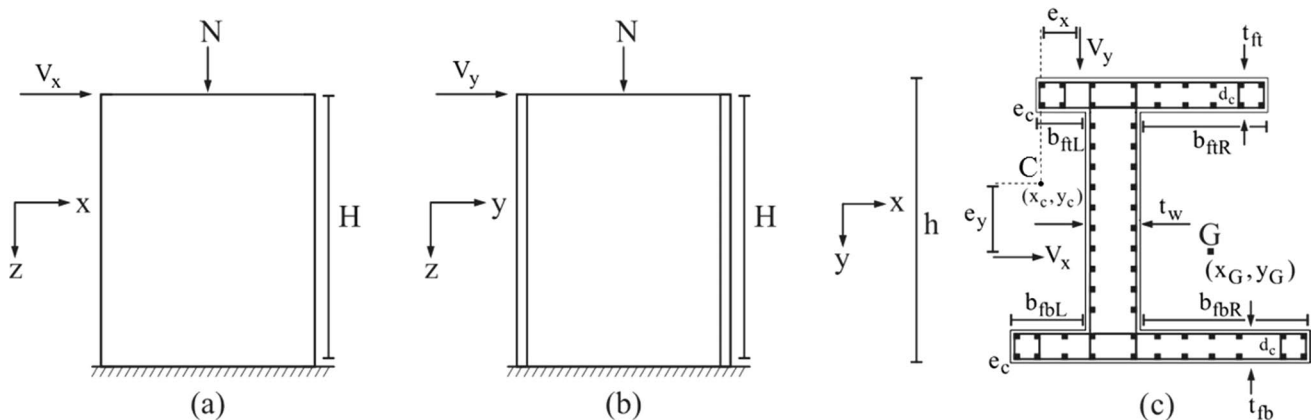


Fig. 2 Schematic view of a non-rectangular RC shear wall (geometry and loading)

- The vertical as well as the out-of-plane shear strains have been neglected in the calculation of the total potential energy function; and
- The equivalent elasticity modulus of the section (E) has been estimated by the approach proposed by Liu et al. [33].

Additionally, the shear modulus, G , is obtained as follows:

$$G = \frac{E}{2(1 + \nu)} \tag{1}$$

wherein ν is Poisson’s ratio of concrete materials ranges between 0.15 and 0.20.

2.2 Determination of the deformation and stress distribution functions

On the strength of the superposition principle, the loads applied to the wall can be decomposed into an axial load imposed to the centroid of the section, two lateral loads applied to the shear center, and also a torsional moment about the z -axis. It is to mention that the torsional moment is calculated as follows:

$$T = V_x e_y - V_y e_x \tag{2}$$

Since the axial load is applied to the centroid of the section, uniform axial deformation and compressive stress appear across the section (Fig. 3a) as follows:

$$u_a(x, y, z) = \frac{N}{AE}(H - z), \tag{3}$$

$$\sigma_a(x, y, z) = -\frac{N}{A}. \tag{4}$$

In Fig. 3b, c, the structure is under the action of two lateral load applied to the shear center of the wall which it bends the structure without any torsion leading to shear stress in the section. Furthermore, due to the non-rectangular

shape of the section, the transfer of shear flow from the flange into the web induces shear-lag and also additional axial and lateral deformations.

In the elastic region, the lateral loads V_x and V_y induce lateral deformations $w_x(z)$ and $w_y(z)$, respectively. These deformations are obtained based on the Bernoulli–Euler assumption, as follows:

$$w_x(z) = \frac{V_x}{6EI_y}(z^3 - 3H^2z + 2H^3), \tag{5}$$

$$w_y(z) = \frac{V_y}{6EI_x}(z^3 - 3H^2z + 2H^3). \tag{6}$$

Let the additional shear-lag induced lateral deformations due to V_x and V_y be s_x and s_y (Fig. 3b, c), respectively. Moreover, $u_{wb}(x, y)$ and $u_{wc}(x, y)$ are the corresponding warping deformations. Thus, the axial deformations function are calculated as follows [44]:

$$u_b(x, y, z) = -\bar{x}(w'_x(z) + s'_x(z)) + u_{wb}(x, y)s'_x(z) = -(x - x_G)w'_x(z) + [u_{wb}(x, y) - x + x_G]s'_x(z), \tag{7}$$

$$u_c(x, y, z) = -\bar{y}(w'_y(z) + s'_y(z)) + u_{wc}(x, y)s'_y(z) = -(y - y_G)w'_y(z) + [u_{wc}(x, y) - y + y_G]s'_y(z) \tag{8}$$

As shown in Fig. 4, to introduce the functions $u_{wb}(x, y)$ and $u_{wc}(x, y)$, a coordinate system with the components of \hat{x} and \hat{y} is defined at the middle height of the section.

Quite a few studies have been conducted to investigate the stress and strain distribution functions in flanged sections due to the shear-lag effect [32–35]. Khaloo et al. [45, 46] conducted an investigation to identify an appropriate function for the shear-lag induced warping deformation. The results of their studies indicated that, among the various proposed functions, the quadratic distribution function, which corresponds to the lateral loading in the x - and y - directions, is the best option for assessing the response of non-rectangular flanged RC shear walls. Therefore, within the framework of the current study,

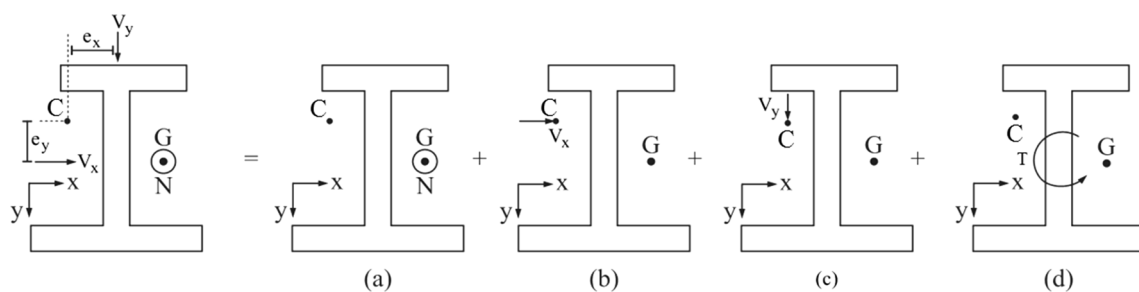


Fig. 3 Decomposition of the loads into a an axial load, b a lateral load in x -direction, c a lateral load in y -direction, and d a torsional moment

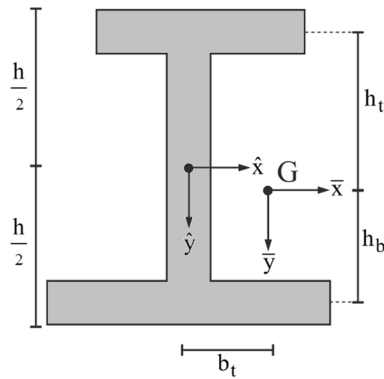


Fig. 4 Coordinate system of a general non-rectangular wall section

the quadratic distribution functions have been proposed in both the x - and y - directions. Therefore, the functions $u_{wb}(\hat{x}, \hat{y})$ and $u_{wc}(\hat{x}, \hat{y})$ can take the following form:

$$u_{wb}(\hat{x}, \hat{y}) = \beta_x - \alpha_x b_t \left(\frac{|\hat{y} - \frac{h}{2} + t_{fb}| |\hat{y} + \frac{h}{2} - t_{ft}|}{(\frac{h}{2} - t_{fb})(\frac{h}{2} - t_{ft})} \right) \left(\frac{\langle \hat{y} + \frac{h}{2} - t_{ft} \rangle}{\hat{y} + \frac{h}{2} - t_{ft}} \right) \left(1 - \frac{\langle \hat{y} - \frac{h}{2} + t_{fb} \rangle}{\hat{y} - \frac{h}{2} + t_{fb}} \right) \tag{9}$$

$$u_{wc}(\hat{x}, \hat{y}) = \beta_y + \alpha_y h_b \left(1 - \left(\frac{\hat{x} - \frac{t_w}{2}}{b_{fbR}} - 1 \right)^2 \right) \left(\frac{\langle \hat{y} - \frac{h}{2} + t_{fb} \rangle}{\hat{y} - \frac{h}{2} + t_{fb}} \right) \left(\frac{\langle \hat{x} - \frac{t_w}{2} \rangle}{\hat{x} - \frac{t_w}{2}} \right) + \alpha_y h_b \left(1 - \left(\frac{\hat{x} + \frac{t_w}{2}}{b_{fbL}} + 1 \right)^2 \right) \left(\frac{\langle \hat{y} - \frac{h}{2} + t_{fb} \rangle}{\hat{y} - \frac{h}{2} + t_{fb}} \right) \left(1 - \frac{\langle \hat{x} + \frac{t_w}{2} \rangle}{\hat{x} + \frac{t_w}{2}} \right) - \alpha_y h_t \left(1 - \left(\frac{\hat{x} - \frac{t_w}{2}}{b_{ftR}} - 1 \right)^2 \right) \left(1 - \frac{\langle \hat{y} + \frac{h}{2} - t_{ft} \rangle}{\hat{y} + \frac{h}{2} - t_{ft}} \right) \left(\frac{\langle \hat{x} - \frac{t_w}{2} \rangle}{\hat{x} - \frac{t_w}{2}} \right) - \alpha_y h_t \left(1 - \left(\frac{\hat{x} + \frac{t_w}{2}}{b_{ftL}} + 1 \right)^2 \right) \left(1 - \frac{\langle \hat{y} + \frac{h}{2} - t_{ft} \rangle}{\hat{y} + \frac{h}{2} - t_{ft}} \right) \left(1 - \frac{\langle \hat{x} + \frac{t_w}{2} \rangle}{\hat{x} + \frac{t_w}{2}} \right) \tag{10}$$

wherein $\langle f \rangle$ represents the Macaulay bracket. If f admits a negative value, the output of the bracket is zero; otherwise, the bracket output is the absolute value of f . In the elastic region, the axial stress distributions are calculated as follows:

$$\sigma_b = E \frac{\partial u_b(x, y, z)}{\partial z} = -E(x - x_G)w_x''(z) + E[u_{wb}(x, y) - x + x_G]s_x''(z), \tag{11}$$

$$\sigma_c = E \frac{\partial u_c(x, y, z)}{\partial z} = -E(y - y_G)w_y''(z) + E[u_{wc}(x, y) - y + y_G]s_y''(z). \tag{12}$$

With the absence of the axial load, one can write as follows:

$$\int_A \sigma_b dA = 0 \rightarrow \int_A (-E(x - x_G)w_x''(z) + E[u_{wb}(x, y) - x + x_G]s_x''(z))dA = 0, \tag{13}$$

$$\int_A \sigma_c dA = 0 \rightarrow \int_A (-E(y - y_G)w_y''(z) + E[u_{wc}(x, y) - y + y_G]s_y''(z))dA = 0. \tag{14}$$

Additionally,

$$\int_A (x - x_G)dA = 0, \tag{15}$$

$$\int_A (y - y_G)dA = 0. \tag{16}$$

Employing Eqs. (15) and (16) for simplification of Eqs. (13) and (14) admits the following:

$$\int_A u_{wb}(x, y) dA = 0, \tag{17}$$

$$\int_A u_{wc}(x, y) dA = 0. \tag{18}$$

Moreover, the bending moment about \bar{x} - and \bar{y} - axes can be found as follows:

$$\int_A \sigma_b(x - x_G) dA = M_{\bar{y}}, \tag{19}$$

$$\int_A \sigma_c(y - y_G) dA = M_{\bar{x}}. \tag{20}$$

Furthermore, it should be noted that:

$$\int_A -E(x - x_G)^2 w_x''(z) dA = M_{\bar{y}}, \tag{21}$$

$$\int_A -E(y - y_G)^2 w_y''(z) dA = M_{\bar{x}}. \tag{22}$$

Within the same approach, Eqs. (19) and (20) can take the following simplified forms:

$$\int_A E[u_{wb}(x, y) - x + x_G] s_x''(z)(x - x_G) dA = 0, \tag{23}$$

$$\int_A E[u_{wc}(x, y) - y + y_G] s_y''(z)(y - y_G) dA = 0 \tag{24}$$

or, equivalently:

$$\int_A u_{wb}(x, y)(x - x_G) dA = \int_A (x - x_G)^2 dA = \bar{I}_y, \tag{25}$$

$$\int_A u_{wc}(x, y)(y - y_G) dA = \int_A (y - y_G)^2 dA = \bar{I}_x. \tag{26}$$

The constants α_x , β_x , α_y , and β_y can be calculated using Eqs. (17), (18), (25), and (26). Also, the total potential energy function is found to be as follows:

$$\Pi = U_{ft} + U_{fb} + U_w + V_L = \int_0^H \int_A \left(\frac{\sigma^2}{2E} + \frac{\tau^2}{2G} \right) dAdz + V_L. \tag{27}$$

Furthermore, I_{wb} , I_{wc} , I_{eb} , and I_{ec} are introduced herein as follows:

$$I_{wb} = \int_A (u_{wb}(x, y) - x + x_G)^2 dA, \tag{28}$$

$$I_{wc} = \int_A (u_{wc}(x, y) - y + y_G)^2 dA, \tag{29}$$

$$I_{eb} = \int_A \left(\frac{\partial u_{wb}(x, y)}{\partial y} \right)^2 dA, \tag{30}$$

$$I_{ec} = \int_A \left(\frac{\partial u_{wc}(x, y)}{\partial x} \right)^2 dA. \tag{31}$$

As a result, the total potential energy function of the wall is obtained as [47] as follows:

$$\begin{aligned} \Pi_b &= \int_0^H \int_A \left(\frac{1}{2} E \left(\frac{\partial u_b}{\partial z} \right)^2 + \frac{1}{2} G \left(\frac{\partial u_b}{\partial y} \right)^2 \right) dAdz + V_{Lb} \\ &= \int_0^H \frac{1}{2} E \bar{I}_y (w_x''(z))^2 dz + \int_0^H \frac{1}{2} E I_{wb} (s_x''(z))^2 dz \\ &\quad + \int_0^H \frac{1}{2} G I_{eb} (s_x'(z))^2 dz + V_{Lb}, \end{aligned} \tag{32}$$

$$\begin{aligned} \Pi_c &= \int_0^H \int_A \left(\frac{1}{2} E \left(\frac{\partial u_c}{\partial z} \right)^2 + \frac{1}{2} G \left(\frac{\partial u_c}{\partial x} \right)^2 \right) dAdz + V_{Lc} \\ &= \int_0^H \frac{1}{2} E \bar{I}_x (w_y''(z))^2 dz + \int_0^H \frac{1}{2} E I_{wc} (s_y''(z))^2 dz \\ &\quad + \int_0^H \frac{1}{2} G I_{ec} (s_y'(z))^2 dz + V_{Lc}, \end{aligned} \tag{33}$$

where V_{Lb} and V_{Lc} are the potential energy values corresponding to the external loadings applied to the section in the x - and y -directions, respectively. These values are identical to the work accomplished by the external loads with the opposite sign ($V = -W$), calculated as follows:

$$V_{Lb} = -V_x(w_x(0) + s_x(0)), \tag{34}$$

$$V_{Lc} = -V_y(w_y(0) + s_y(0)). \tag{35}$$

In order to minimize the total potential energy functions Π_b and Π_c , it is suffice to set $\delta \Pi_b$ and $\delta \Pi_c$ equal to zero:

$$\begin{aligned} \delta\Pi_b = & \int_0^H E\bar{I}_y w_x''''(z) \delta w_x(z) dz + E\bar{I}_y w_x''(z) \delta w_x'(z) \Big|_0^H \\ & - E\bar{I}_y w_x'''(z) \delta w_x(z) \Big|_0^H + \int_0^H (EI_{wb} s_x''''(z) \\ & - GI_{eb} s_x''(z)) \delta s_x(z) dz + EI_{wb} s_x''(z) \delta s_x'(z) \Big|_0^H \\ & - EI_{wb} s_x'''(z) \delta s_x(z) \Big|_0^H + GI_{eb} s_x'(z) \delta s_x(z) \Big|_0^H \\ & - V_x [\delta w_x(0) + \delta s_x(0)] = 0, \end{aligned} \tag{36}$$

$$\begin{aligned} s_y(z) = & \frac{V_y H}{EI_{wc} \lambda_c^2} - \frac{V_y}{EI_{wc} \lambda_c^3} \tan h(\lambda_c H) - \frac{V_y z}{EI_{wc} \lambda_c^2} \\ & + \frac{V_y}{EI_{wc} \lambda_c^3 \cos h(\lambda_c H)} \sin h(\lambda_c z). \end{aligned} \tag{47}$$

Substituting Eqs. (46) and (47) into Eqs. (11) and (12) gives the axial stress distribution function. Then, the axial deformation and stress distribution under the action of torsional moment (Fig. 3d) are computed. Based on the

$$\begin{aligned} \delta\Pi_c = & \int_0^H E\bar{I}_x w_y''''(z) \delta w_y(z) dz + E\bar{I}_x w_y''(z) \delta w_y'(z) \Big|_0^H - E\bar{I}_x w_y'''(z) \delta w_y(z) \Big|_0^H \\ & + \int_0^H (EI_{wc} s_y''''(z) - GI_{ec} s_y''(z)) \delta s_y(z) dz + EI_{wc} s_y''(z) \delta s_y'(z) \Big|_0^H \\ & - EI_{wc} s_y'''(z) \delta s_y(z) \Big|_0^H + GI_{ec} s_y'(z) \delta s_y(z) \Big|_0^H - V_y [\delta w_y(0) + \delta s_y(0)] = 0. \end{aligned} \tag{37}$$

As a result, the additional shear-lag induced displacements in x - and y -directions are, respectively, derived as follows:

$$EI_{wb} s_x''''(z) - GI_{eb} s_x''(z) = 0, \tag{38}$$

$$EI_{wc} s_y''''(z) - GI_{ec} s_y''(z) = 0. \tag{39}$$

For $\lambda_b = \sqrt{GI_{eb}/EI_{wb}}$ and $\lambda_c = \sqrt{GI_{ec}/EI_{wc}}$:

$$s_x''''(z) - \lambda_b^2 s_x''(z) = 0, \tag{40}$$

$$s_y''''(z) - \lambda_c^2 s_y''(z) = 0. \tag{41}$$

The general solutions of Eqs. (40) and (41) are as follows:

$$s_x(z) = k_{1x} + k_{2x}z + k_{3x} \cosh(\lambda_b z) + k_{4x} \sinh(\lambda_b z), \tag{42}$$

$$s_y(z) = k_{1y} + k_{2y}z + k_{3y} \cosh(\lambda_c z) + k_{4y} \sinh(\lambda_c z). \tag{43}$$

Furthermore, both the initial and boundary conditions in x - and y -directions of the wall are, respectively, given as follows:

$$s_x''(0) = 0, \quad s_x'''(0) - \lambda_b^2 s_x'(0) = \frac{V_x}{EI_{wb}}, \quad s_x(H) = s_x'(H) = 0, \tag{44}$$

$$s_y''(0) = 0, \quad s_y'''(0) - \lambda_c^2 s_y'(0) = \frac{V_y}{EI_{wc}}, \quad s_y(H) = s_y'(H) = 0. \tag{45}$$

Thus, the additional lateral deformations due to the shear deformation are obtained as follows:

$$s_x(z) = \frac{V_x H}{EI_{wb} \lambda_b^2} - \frac{V_x}{EI_{wb} \lambda_b^3} \tan h(\lambda_b H) - \frac{V_x z}{EI_{wb} \lambda_b^2} + \frac{V_x}{EI_{wb} \lambda_b^3 \cosh(\lambda_b H)} \sin h(\lambda_b z). \tag{46}$$

Vlasov's torsion theory [48], the rotation ϕ of the section due to the torsional moment T admits the following:

$$EC_w \phi''''(z) - GJ \phi''(z) = 0, \tag{48}$$

where C_w is the warping constant defined as follows:

$$C_w = \int_A \Psi^2 dA, \tag{49}$$

in which Ψ is the warping function defined for open sections as follows:

$$\Psi = \int_s h ds - \frac{1}{A} \int_A \int_s h ds dA, \tag{50}$$

where h is the vertical distance of an arbitrary point in the section from the shear center. By substituting $\lambda_t = \sqrt{GJ/EC_w}$, Eq. (48) can be simplified as follows:

$$\phi''''(z) - \lambda_t^2 \phi''(z) = 0 \tag{51}$$

and then, the integration of Eq. (51) along the height of the wall gives the following:

$$\phi'''(z) - \lambda_t^2 \phi'(z) = \frac{T}{EC_w}. \tag{52}$$

Therefore, the general solution of Eq. (52) is given as follows:

$$\phi(z) = k_1 + k_2 z + k_3 \cos h(\lambda_t z) + k_4 \sin h(\lambda_t z). \tag{53}$$

Based on the boundary conditions of the wall and a fixed support at $z = H$, the solution of Eq. (54) yields the following:

$$\phi(z) = \frac{-T}{EC_w \lambda_t^3} (\tan h(\lambda_t H) \cos h(\lambda_t(H-z)) - \tan h(\lambda_t H) - \sin h(\lambda_t(H-z)) + \lambda_t(H-z)). \tag{54}$$

With the known value of ϕ , the axial deformation and stress distribution due to the warping torsion can be calculated as follows:

$$u_d(x, y, z) = -\frac{d\phi}{dz} \Psi, \tag{55}$$

$$\sigma_d(x, y, z) = -E \frac{d^2\phi}{dz^2} \Psi. \tag{56}$$

The bi-moment B is defined as follows:

$$B = -EC_w \frac{d^2\phi}{dz^2}. \tag{57}$$

Therefore, employing Eq. (58), the axial stress distribution function takes the following form:

$$\sigma_d(x, y, z) = \frac{B}{C_w} \Psi. \tag{58}$$

Hence, with the known functions of $u_a, u_b, u_c, u_d, \sigma_a, \sigma_b, \sigma_c,$ and σ_d , the axial deformation and stress arising from the shear-lag and warping torsion can be obtained as follows:

$$u(x, y, z) = u_a(x, y, z) + u_b(x, y, z) + u_c(x, y, z) + u_d(x, y, z), \tag{59}$$

$$\sigma(x, y, z) = \sigma_a(x, y, z) + \sigma_b(x, y, z) + \sigma_c(x, y, z) + \sigma_d(x, y, z). \tag{60}$$

Provided in Fig. 5 are the conventional non-rectangular sections, including Z-, T-, I-, C- and L-shaped sections which can be attained introducing appropriate geometrical properties into the general section defined in this study.

2.3 Discussion of the coefficients and constants

The axial stress distribution along with the pre-cracking deformation functions can be calculated under the simultaneous action of the shear-lag and warping torsion employing the coefficients established in the previous sub-section. Further details on the definition and calculation of the above-described parameters such as warping constant, Bi-moment, and shear center can be found in a number of studies [38, 49–54]. For the purpose of convenience, the coefficients of the shear-lag and their corresponding expressions are provided in the Appendix of the paper. It should be noted that, in the special case of b_t equal to zero, α_x has not been defined which means that the shear-lag may not even take place for the section (i.e., a rectangular section). Nevertheless, in other cases in which the shear-lag influence can be meaningful, it is required to incorporate $\alpha_x b_t$ into γ_t . It is worth noting that β_x is assumed to be zero about the vertical axis of symmetric sections (\hat{y} in Fig. 4). In the case of ambiguity for the other coefficients, the basic definitions of the previous section should be utilized.

In general, based on the importance and type of the structure and in order to restrict its lateral deformation, RC shear wall can be an efficient option, whose dimension and reinforcement detailing are oftentimes determined with a conservation in the design process. Therefore, in many cases, the RC wall remains within the elastic region, i.e.,

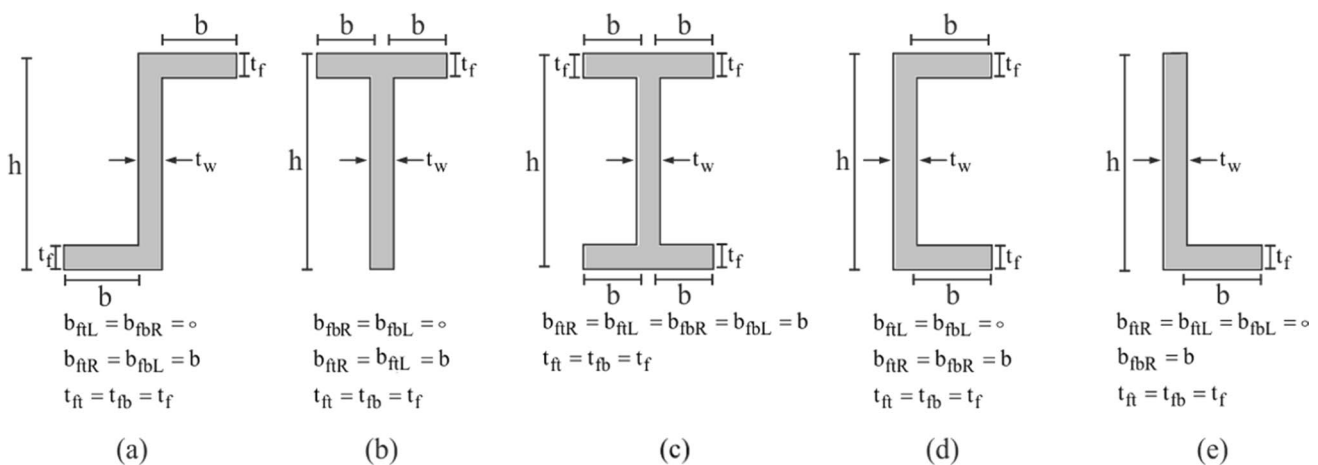


Fig. 5 The geometrical characteristics of a Z-shaped, b T-shaped, c I-shaped, d U-shaped, and e L-shaped sections

before onset of cracking, under different lateral loading scenarios. With this in view, the equations described in Sect. 2.2 can essentially be applied in these scenarios to control the stresses and lateral deformation of the walls.

Nevertheless, in real earthquakes, the seismic wave can essentially reach structures from any direction, which necessitates examining the seismic performance of non-rectangular flanged RC shear walls subjected to the action of various lateral loading directions [14, 55, 56]. In some cases, in which the seismic loading is less than the cracking load of the non-rectangular flanged RC shear walls, the equations established in the Sect. 2.2, and those provided in the Appendix section can be employed to control the above-mentioned criterion. Therefore, the succeeding sub-section is devoted to evaluate the cracking load of non-rectangular flanged RC shear walls.

2.4 Cracking load

For the case of the Bernoulli–Euler assumption, wherein the shear-lag and warping torsion have not been involved in the formulation, the stress distribution of the section is calculated as follows:

$$\sigma(x, y, z) = -\frac{V_x z \bar{x}}{\bar{I}_y} - \frac{V_y z \bar{y}}{\bar{I}_x} - \frac{N}{A} \tag{61}$$

For positive values of V_x and V_y , and also for the lack of cracks under the applied loadings, the following is required:

$$\frac{V_x H h_1}{\bar{I}_y} + \frac{V_y H h_2}{\bar{I}_x} - \frac{N}{A} < f'_t \tag{62}$$

in which f'_t is the tensile strength of concrete, h_1 and h_2 have been defined as depicted in Fig. 6. Therefore, for V_x and V_y

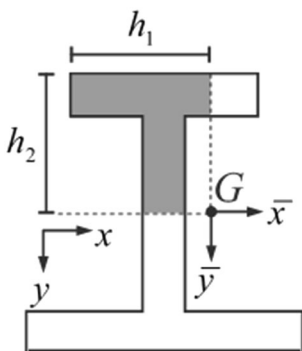


Fig. 6 Tensioned area of the section

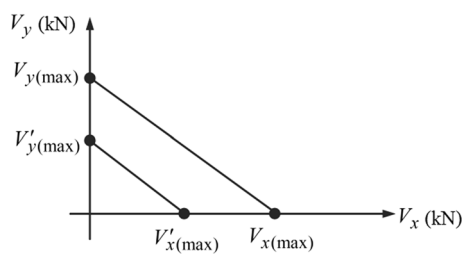


Fig. 7 Comparison of the shear-lag effect on the cracking curves

values under cracking condition, a linear curve is achieved (Fig. 7), wherein $V_{x(max)}$ and $V_{y(max)}$ are obtained as follows:

$$V_{x(max)} = \frac{\bar{I}_y}{H h_1} \left(f'_t + \frac{N}{A} \right), \tag{63}$$

$$V_{y(max)} = \frac{\bar{I}_x}{H h_2} \left(f'_t + \frac{N}{A} \right). \tag{64}$$

However, when the shear-lag and warping torsion are considered in the calculation of cracking loads, this curve may be nonlinear depending on the location where the loads are applied to the section. In this case, the curve is determined employing Eq. (60) and also the inequality of $\sigma(x, y, z) < f'_t$. Furthermore, $V'_{x(max)}$ and $V'_{y(max)}$ are calculated using the former inequality. It should be noted that, in the example provided below, the cracking curve of a U-shaped section is numerically and analytically derived, and the difference between the results of those and the linear curve obtained from Eq. (62) has been evaluated.

3 Validation of the analytical formulation

3.1 Numerical example

This section numerically investigates a non-rectangular RC shear wall to validate the proposed analytical formulations. Previous studies employed T- and I-shaped sections for validation of the analytical equations addressed in the literature [33–35]; However, in this study, a U-shaped section has numerically been examined.

In the experimental investigation performed by Beyer et al. [30], two U-shaped walls were studied under the quasi-static loading. In addition, Constantin and Beyer [13] evaluated the seismic performance of U-shaped RC shear walls under diagonal quasi-static loadings. It is to mention that the walls had been reinforced with asymmetric longitudinal reinforcements. In the current study, the geometry

Fig. 8 Geometry and reinforcement configurations of the numerical example: **a** configurations of longitudinal and transverse reinforcement bars, **b** lateral loads, and **c** axial distributed load (All dimensions are in cm) [13]

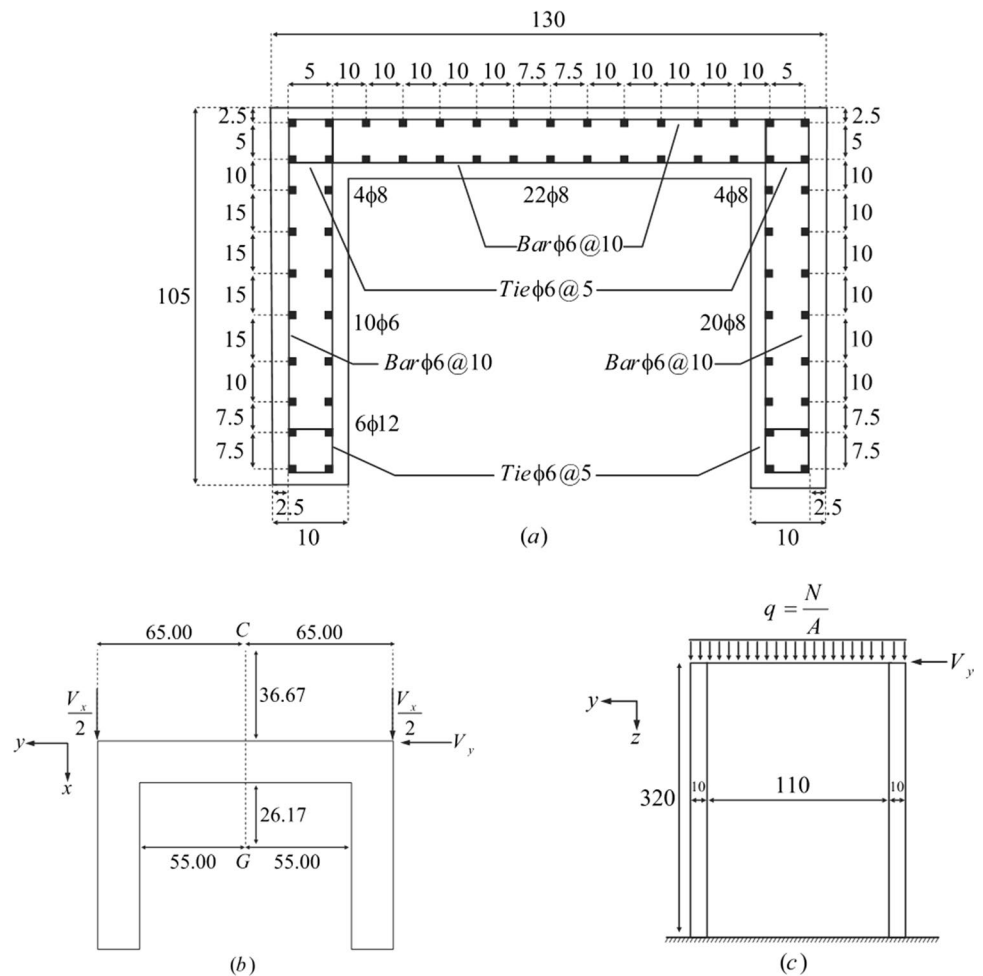


Table 1 Mechanical properties of TUD [13]

Parameter	Value
Characteristic strength, f'_c	37.0 ± 1.3 MPa
Modulus of elasticity, E_c	30.3 ± 0.8 GPa
Tensile strength, f'_t	3.0 ± 0.2 MPa

Table 2 Mechanical properties of reinforcement bars in TUD [13]

Bar diameter	$\epsilon_{su}(\%)$	f_y (MPa)	f_u (MPa)	f_u/f_y
$\phi 6$	6.8 ± 0.9	492 ± 5.1	623 ± 8.7	1.26 ± 0.02
$\phi 8$	7.9 ± 0.8	563 ± 26.6	663 ± 6.5	1.18 ± 0.05
$\phi 12$	9.6 ± 1.2	529 ± 4.7	633 ± 3.9	1.19 ± 0.01

and reinforcement detailing of the numerical example were adopted from the TUD sample of the above-mentioned study to assess the effects of asymmetry reinforcements on the accuracy of the proposed analytical equations. It should be noted that the configuration of the transverse reinforcements in the confined area, boundary conditions, and also the loading pattern slightly differ from Ref. [13]. In what follows, the present study attempts to evaluate the U-shaped wall before the onset of cracking (Fig. 8).

Tables 1 and 2, respectively, summarize the mechanical properties of concrete materials and steel reinforcements.

As shown in Fig. 9, in order to simulate the confined concrete under compression, Roy and Sozen’s model [57] has been adopted. Also, the strain corresponding to $0.5f'_c$

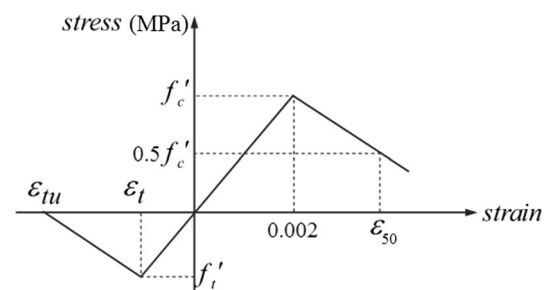


Fig. 9 Stress–strain curve of the confined concrete

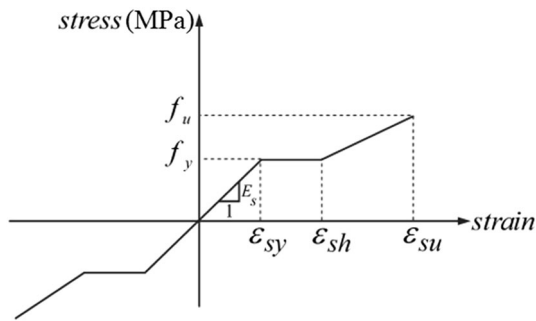


Fig. 10 Stress–strain curve of the steel reinforcement

Table 3 Coefficients of the U-shaped wall

Parameter	Value	Parameter	Value	Parameter	Value
E (GPa)	33.300	h_t (m)	0.6	α_y	1.905
G (GPa)	14.400	h_b (m)	0.6	I_{wb} (m ⁴)	0.066
λ_b (1/m)	2.775	\bar{I}_x (m ⁴)	0.087	I_{wc} (m ⁴)	0.046
λ_c (1/m)	1.867	\bar{I}_y (m ⁴)	0.036	I_{eb} (m ⁴)	1.181
λ_t (1/m)	0.226	J (m ⁴)	0.001	I_{ec} (m ⁴)	0.367
C_w (m ⁶)	0.009	β_x (m)	0.358	\hat{x}_c (m)	-0.367
x_G (m)	0.312	β_y (m)	0	\hat{y}_c (m)	0
y_G (m)	0	α_x	5.006	A (m ²)	0.320

was utilized proportional to the transverse reinforcement. Furthermore, the bilinear model is employed to model the tensile behavior of concrete materials.

To simulate the behavior of the steel reinforcements, the tri-linear curve has been adopted in both tension and compression regions which is shown in Fig. 10 [58].

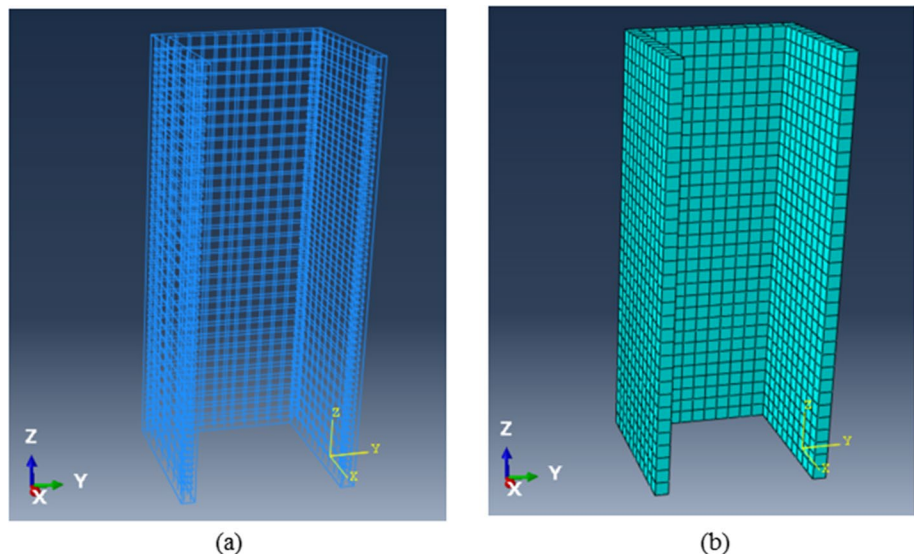
Also, based on the previously established formulations, the coefficients of the U-shaped wall are summarized in Table 3.

The distribution of the axial stress in the elastic region is the same as the case where a concentrated load V_x is applied to the section at the axis of symmetry of the section. To evaluate behavior of the shear wall under different loading conditions, the numerical example has been simulated in ABAQUS software. First, the geometry and material properties are introduced into ABAQUS, and then, the fixed-support boundary conditions are employed to one end. In the next step, the lateral loads have been applied to the wall. Figure 11 depicts the configuration of the steel reinforcement along with the mesh of the wall.

Moreover, the eight-node hexahedral element (C3D8R) has been employed for the modelling of concrete materials. For steel reinforcements (longitudinal and transverse), three-dimensional two nodes truss element (T3D2) is assigned in the FE analyses and all the reinforcements have been embedded in the concrete materials. In order to identify appropriate mesh properties, extensive mesh studies were performed which indicated that assigning element size of 10 cm for simulation of the concrete materials and steel reinforcements in the elastic region is satisfactory with due attention to the accuracy of the results and running time.

Figure 12 illustrates the axial stress distribution and axial deformation contour for the U-shaped RC shear wall under examination subjected to the axial and lateral loadings in the x - and y -directions. As the results presented in this figure suggest, the distribution of axial stress as well as axial deformation is essentially nonlinear. The reason behind this observation stems from the nonlinearity effects introduced by the shear-lag phenomenon along the height of the wall due to the action of lateral loadings V_x and V_y .

Fig. 11 Simulation of the U-shaped RC shear wall in ABAQUS software: **a** configuration of the steel reinforcements, and **b** wall meshes



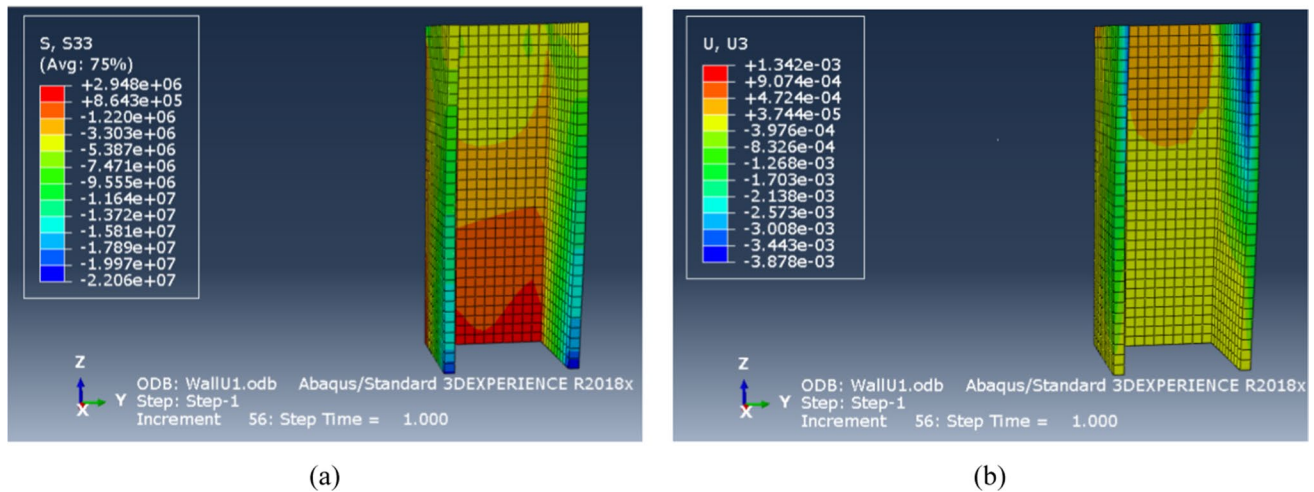


Fig. 12 Contours of the following: **a** axial stress distribution, and **b** axial deformation of the U-shaped RC shear wall

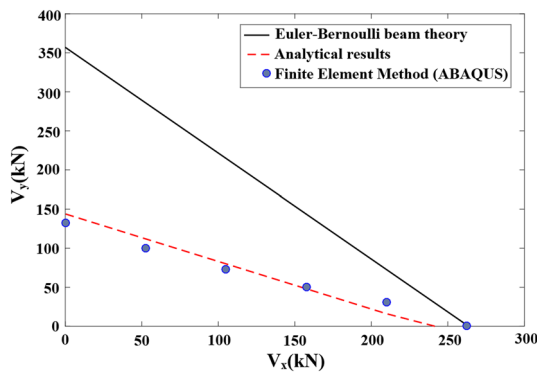


Fig. 13 Comparison of the cracking load curves

In this study, the U-shaped shear wall was subjected to six different load combinations with different values of V_x and V_y up to the onset of cracking to investigate the axial deformation and stress distribution. The results attained by the FE method has then been compared with those of the analytical one.

3.2 Comparison of the results

In this sub-section, to further evaluate the efficiency of the proposed analytical solution, response parameters in terms of the cracking loads, axial deformation, and axial stress distribution are obtained. Then, the results attained by the proposed analytical formulation are compared with the FE simulation as well as the solution based on the Bernoulli–Euler assumption. Figure 13 depicts the variation of the cracking loads through applying the above-mentioned methods.

According to Fig. 13, the numerical results are significantly different from those obtained employing the Bernoulli–Euler assumption. Moreover, this difference can be negligible, i.e., less than 0.5%, only when V_x is applied to the wall. However, the discrepancy increases when V_y has been applied to the wall. This observation can be addressed to the fact that the shear-lag and warping torsion occur in both directions. Also, the numerical value of $V_{y(max)}$ is less than half of the value achieved based on the Bernoulli–Euler assumption under cracking conditions. However, the numerical results are in good agreement with those of the proposed analytical approach, and average difference of less than 8% has been achieved. It should be noted that, all the curves plotted in Fig. 13 are linear due to the point that, for these cases, the maximum tensile stress takes place at an identical position on the section.

Figure 14 compares the results estimated by the Bernoulli–Euler assumption, proposed analytical equations, and numerical simulation in terms of the axial stress distribution and axial deformation for six load combinations. On the basis of the Saint–Venant’s principle and in order to avoid stress concentration, the stress distribution and axial deformation have been measured on sections with adequate distances from the two ends of the wall.

As can be seen in Fig. 14, the analytical equations exhibit favorable accuracy in the estimation of the values and variations of the axial stress as well as the axial deformation under different loadings. Furthermore, by comparing the analytical axial deformation with the FE results, less than 5% error can be observed. Similarly, corresponding error for the estimation of the axial stress is approximately 10%. These errors can be attributed to the assumption of a homogeneous wall structure and also employing the last assumption introduced in Sect. 2. The equivalent modulus of elasticity

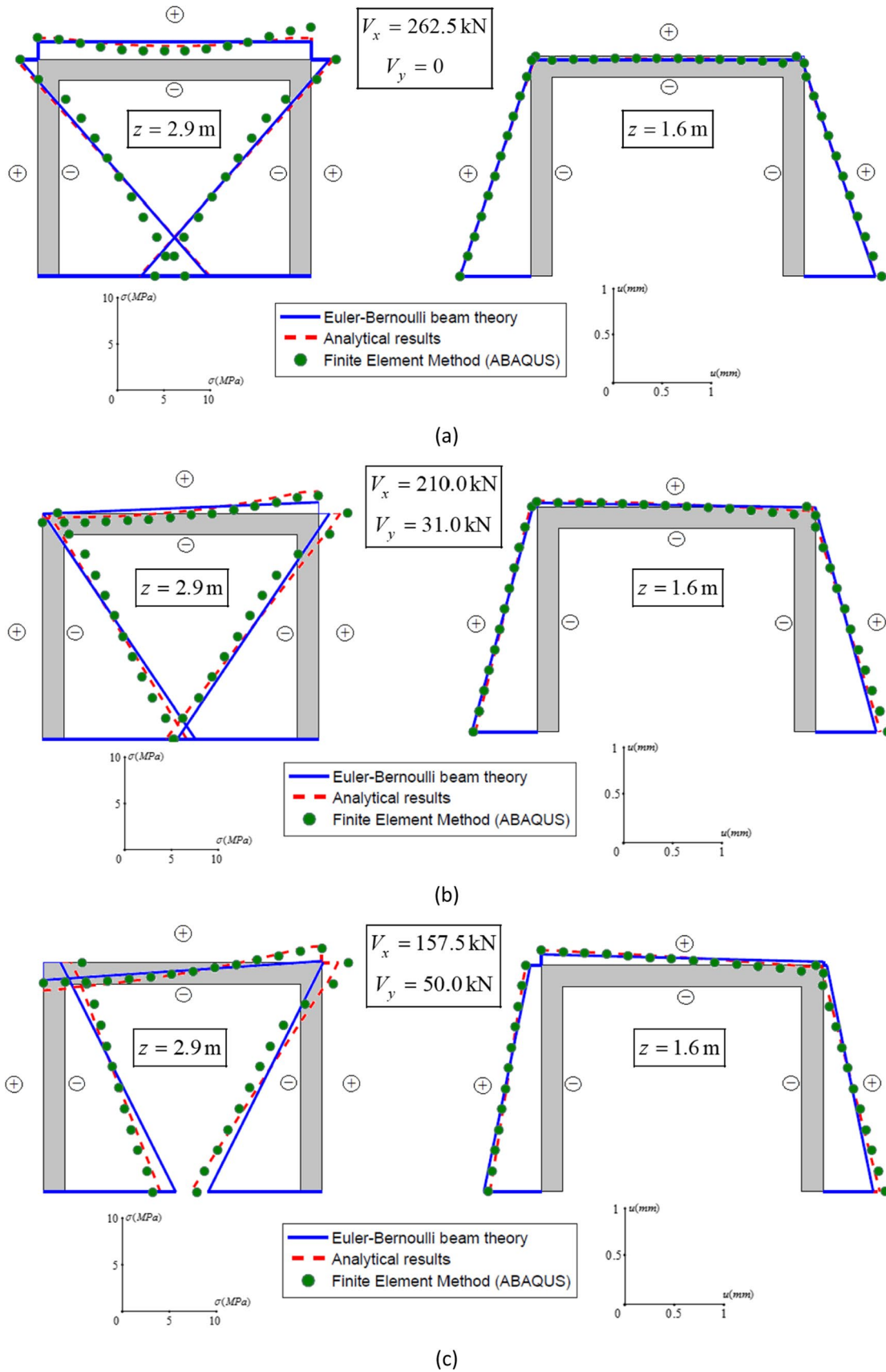
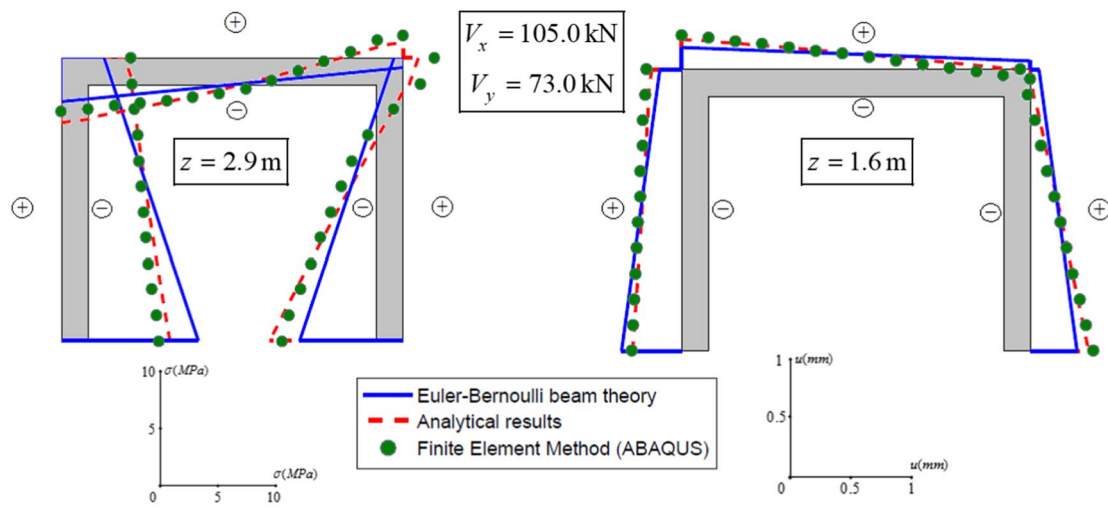
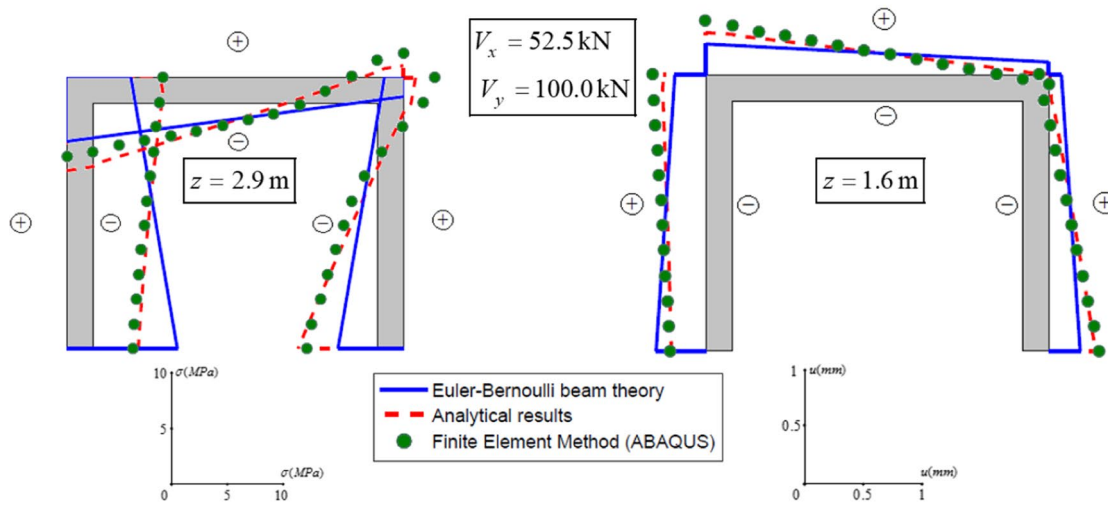


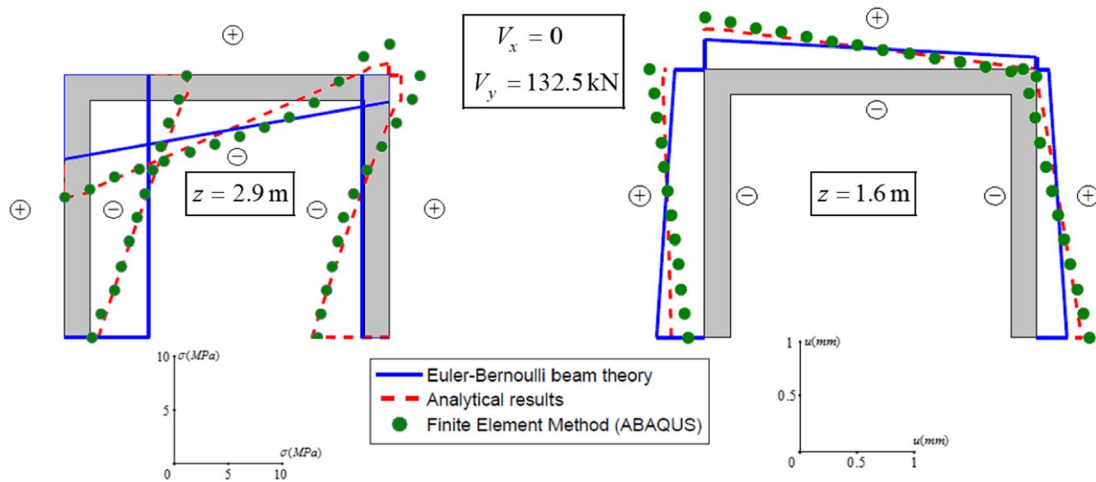
Fig. 14 Axial stress distribution and deformation comparison of the Bernoulli–Euler assumption, proposed analytical method, and FE results



(d)



(e)



(f)

Fig. 14 (continued)

of the wall in the elastic range is estimated through the transformed section analysis. It should be noted that, the shear wall was assumed to be symmetric in the analysis; however, the two flanges possess different configurations of the steel reinforcements. According to Fig. 14, and by recourse to the assumption made in Refs. [33–35], to predict the axial deformation and stress distribution of a RC shear wall in the linear region, it is reasonable to employ the equivalent modulus of elasticity and analyze the effects of the shear-lag, assuming a homogenous section before onset of cracking.

4 Discussion of the analytical results

The analytical formulation established in this study was demonstrated to offer favorable performance in the response prediction of non-rectangular RC shear walls under bi-directional loadings. In this section, the contribution of the induced shear-lag and warping torsion is discussed in detail into the axial deformation and stress distribution of a U-shaped RC shear wall.

In that regard, to investigate the simultaneous effects of the shear-lag and warping torsion on U-shaped RC shear walls, the non-dimensional parameter, μ_s , is defined herein as the ratio of the maximum tensile stress stems from the simultaneous actions of the shear-lag and warping torsion to the maximum induced tensile stress due to the Bernoulli–Euler assumption. Figure 15 demonstrates the variation of μ_s for different lateral loadings applied to the section and different levels along the height of wall in the absence of the axial loading.

As shown in Fig. 8b, the lateral loadings have been imposed to the wall. As Fig. 15 suggests, when the lateral

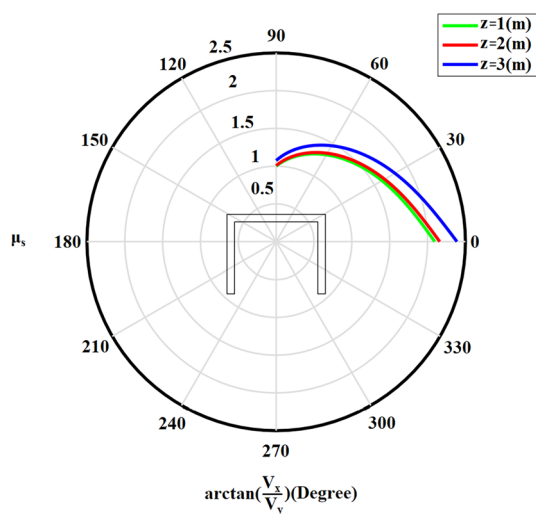


Fig. 15 Variation of μ_s for different lateral loads and levels along the height of the wall

loading is applied only in x -direction, the maximum tensile stress experienced by the structure has been increased up to 10% owing to the shear-lag effect. However, in the case that the lateral load has been applied in y -direction, due to the simultaneous effect of the shear-lag and warping torsion, the maximum induced tensile stress becomes more than twice of that of the Bernoulli–Euler assumption.

In what follows, the contribution of the shear-lag in addition to the warping torsion into the augmented values of axial stress is evaluated. It is worthy of mention that the degree of participation essentially depends on the load eccentricity, lateral load ratio, and height of the structure. In order to better address this point, the coefficients μ_{sb} , μ_{sc} , and μ_{sd} denoting, respectively, the contributions of the shear-lag in the x - and y -directions, and warping torsion, are defined herein as follows:

$$\mu_{sb} = \frac{\sigma_b - \bar{\sigma}_b}{\sigma - \bar{\sigma}}, \tag{65}$$

$$\mu_{sc} = \frac{\sigma_c - \bar{\sigma}_c}{\sigma - \bar{\sigma}}, \tag{66}$$

$$\mu_{sd} = \frac{\sigma_d}{\sigma - \bar{\sigma}}, \tag{67}$$

where $\bar{\sigma}_b$, $\bar{\sigma}_c$ and $\bar{\sigma}$ are given as follows:

$$\bar{\sigma}_b = -E(x - x_G)w''_x(z), \tag{68}$$

$$\bar{\sigma}_c = -E(y - y_G)w''_y(z), \tag{69}$$

$$\bar{\sigma} = \bar{\sigma}_b + \bar{\sigma}_c = -E[(x - x_G)w''_x(z) + (y - y_G)w''_y(z)]. \tag{70}$$

Figure 16 depicts the plots of μ_{sb} , μ_{sc} , and μ_{sd} for different values of e_y and also lateral load ratios at $z = 3$ m for the U-shaped RC wall.

As Fig. 16a suggests, the shear-lag effect originating from the lateral loading in x -direction can be ignored under different loading conditions. The shear-lag effect should be considered only when a lateral load is applied to the structure in x -direction. Therefore, in most cases, the exclusion of the shear-lag effect cannot influence the accuracy of the results.

Moreover, a comparison of Fig. 16b, c clearly indicates that the contribution of the shear-lag to the shear stress is larger than that of warping torsion when a lateral loading is applied at a small distance from the shear center (approximately 0.1 m in this case). However, the more the eccentricity of the load in y -direction, the more the participation of the warping torsion in the increased axial stress. It is worth noting that both the shear-lag resulting from the lateral load in y -direction and warping torsion have significant contribution and cannot be ignored in the eccentricity range of

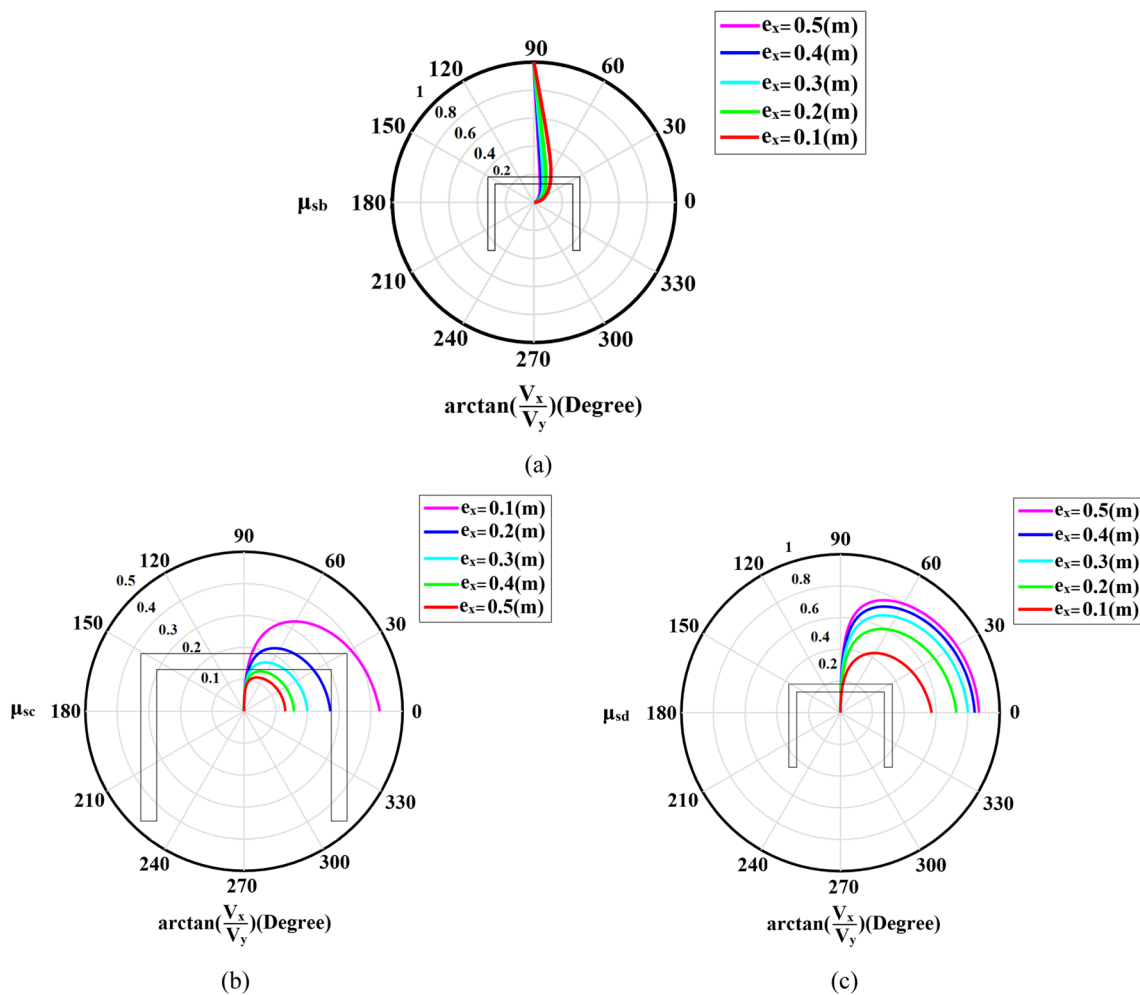


Fig. 16 Variations of: **a** μ_{sb} , **b** μ_{sc} , and **c** μ_{sd} for different values of e_y and lateral load ratios at $z = 3$ m

0.1–0.5 m. Therefore, the exclusion of the above-mentioned components can significantly reduce the accuracy of the results.

Furthermore, it is required to highlight the effect of the shear-lag on the induced additional lateral deformation in the loading direction. In this regard, Fig. 17 exhibits the variations of the additional deformation function along the height of the wall under the action of six load combinations for the U-shaped RC wall.

Figure 18 demonstrates the variation of the rotation angle versus the torsional moment along the height of the structure. A comparison of Figs. 17 and 18 reveals that the general trend of the additional lateral deformations and torsional moment-induced rotation are comparable.

In the following, the shear-lag effect has been highlighted on the drift response of the U-shaped RC shear wall examined in the current study. As the shear-lag can induce additional lateral deformation in the structure, it is important to consider this phenomenon in the drift response of non-rectangular RC shear walls. Hence, Fig. 19 compares the drift

values of the U-shaped wall (Fig. 8) in which the shear-lag effect has been included/excluded under a lateral loading of 100 kN. Comparing two sets of the curves plotted in this figure yields that the shear-lag contribution is not meaningful in the elastic region; however, this effect may be more significant after onset of cracking.

5 Conclusion

This paper analytically investigated the simultaneous effects of the shear-lag and warping torsion on the behavior of non-rectangular RC shear walls. First, a non-rectangular wall with an arbitrary geometry was subjected to the axial as well as the lateral loading, and torsional moment. Thereafter, the axial deformation and stress distribution were formulated within the elastic region with emphasis on the contribution of the shear-lag in conjunction with the warping torsion. In the next step, to validate the analytical equations established in this study, FE simulations of a U-shaped RC shear wall

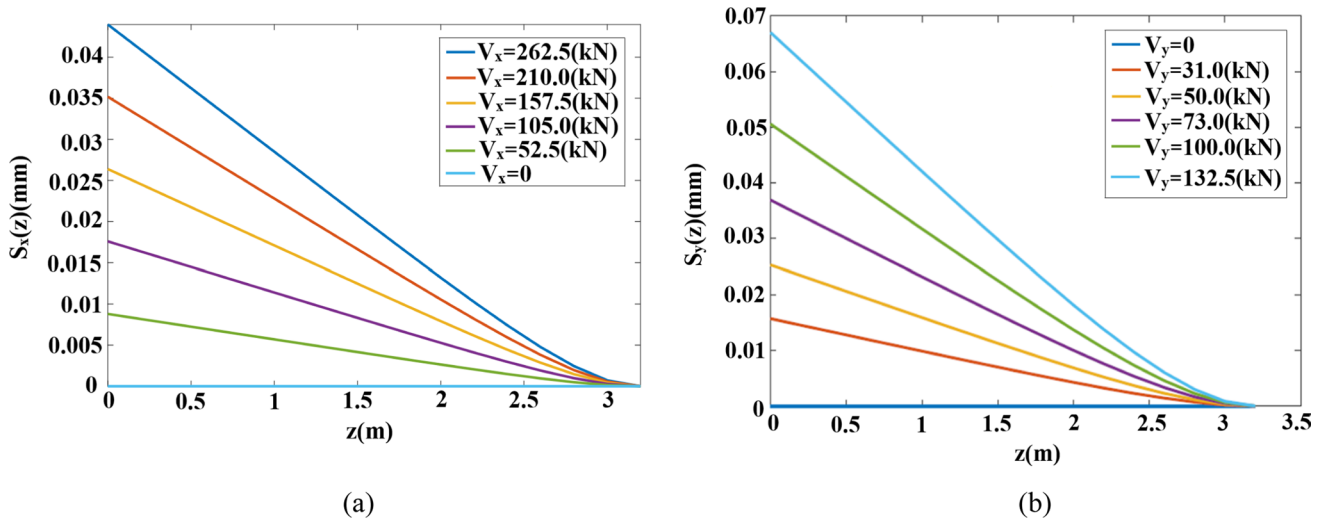


Fig. 17 Additional lateral deformation due to the shear-lag resulting from the lateral loading in **a** x-direction and **b** y-direction

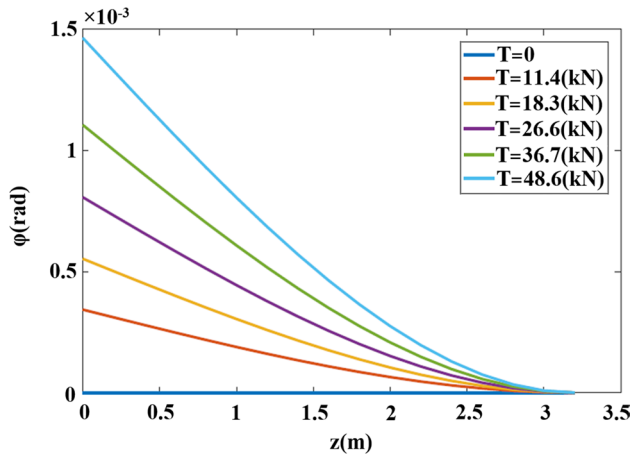


Fig. 18 Variation of the rotation angle due to the applied torsional moments

were carried out in the ABAQUS software. The following findings can be drawn through comparing the analytical formulations with the numerical modeling:

1. The Bernoulli–Euler assumption was not capable to accurately estimate the axial stress distribution of the section, to an extent that, the cracking load was predicted to be up to twice as the case in which the simultaneous effect of shear-lag and warping torsion has been considered.
2. Comparison between the values of cracking load obtained through the analytical and numerical approaches indicated an average of 10% error.
3. The results for the axial deformation and stress distribution reveal that the discrepancy between analytical and computational simulation is approximately 5 and 10%, respectively. The reason behind these disparities can be attributed to the heterogeneity of RC members

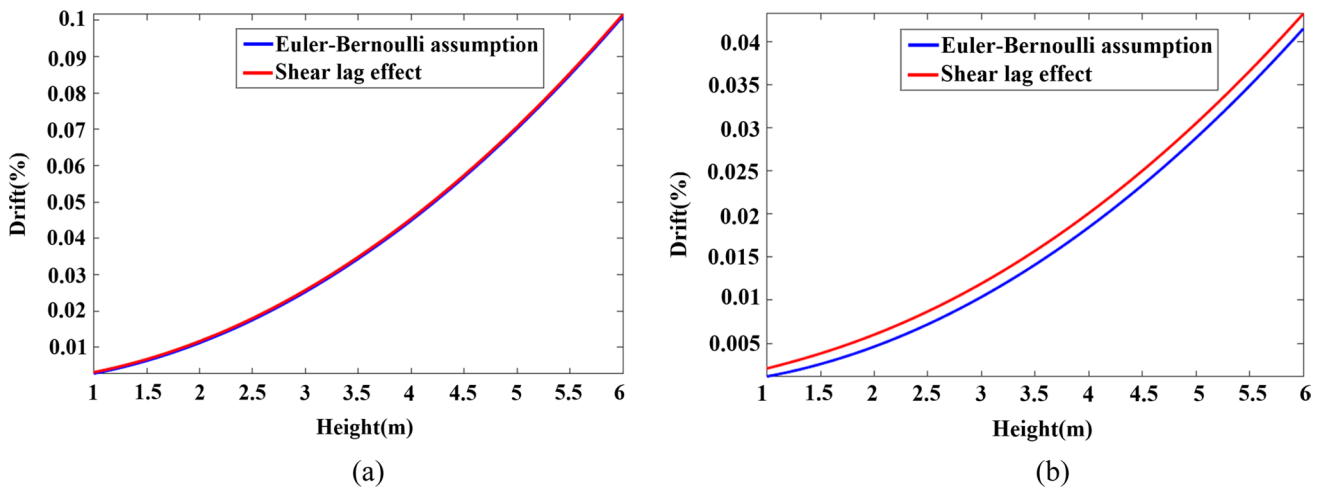


Fig. 19 Shear-lag effect on the drift response of the U-shaped shear wall: **a** x-direction and **b** y-direction

due to the presence of steel reinforcements. In addition, the asymmetric configuration of the reinforcements was not incorporated into the basic assumptions of the analytical equations.

4. The findings of this study demonstrate the inevitable contribution of concurrent effects of the shear-lag and torsional warping on the response of RC shear walls with non-rectangular flanged sections. In addition, ignoring the cumulative effects of the above-mentioned parameters in the study of these structural elements, particularly in RC shear walls with asymmetric cross-section, can offer inaccurate and unreliable results in many cases. Therefore, due to the widespread usage of T-, U-, and L-shaped sections in practice, expressions provided in the Appendix can be employed in the preliminary design of RC shear walls possessing non-rectangular flanged sections.

Moreover, further scrutiny on the analytical formulations for the U-shaped section examined in the current study divulges the following:

1. The shear-lag and warping torsion could significantly alter the stress distribution of non-rectangular RC walls, and the exclusion of those might lead to the underestimation of the maximum tensile stress by up to half.
2. Depending on the load eccentricity, the participation of the shear-lag and warping torsion to the axial stress distribution could be different. For the range of the eccentricities considered in this study, both contribution of the

shear-lag and warping torsion was significant and cannot be ignored in the analysis of U-shaped RC walls.

3. Consideration of the shear-lag can alter the axial deformation as well as the stress distribution of the structure, and also the lateral deformations, and in some cases, the degree of modification was remarkable.
4. The additional lateral deformations introduced by the shear-lag before cracking has insignificant effect on the drift response of U-shaped RC walls; however, it is expected to be more crucial in the inelastic region.

Finally, as there are no specific recommendations in current design codes, wherein the simultaneous impacts of the shear-lag and torsional warping have been taken into account, recourse can be made to adopt a numerical model employing the commercial FE tools in order to provide more accurate response assessment in the analysis and design of RC shear wall with non-rectangular flanges sections.

Appendix

The geometrical properties of a flanged RC shear wall with an arbitrary section are listed in Table 4. Moreover, as RC shear walls with T-, U-, and L-shaped sections are more commonly utilized in comparison with other non-rectangular sections, Tables 5, 6, 7 respectively summarize the coefficients required for computation of the axial deformation and stress distribution of the above-described sections.

Table 4 Coefficients of a general flanged section

Section	Parameter	Expression
General section	A	$(h - t_{ft} - t_{fb})t_w + (b_{flL} + b_{flR} + t_w)t_{ft} + (b_{fbL} + b_{fbR} + t_w)t_{fb}$
	$x_G(b_t)^*$	$\frac{(b_{flL} + b_{flR} + t_w)(b_{flR} - b_{flL})t_{ft} + (b_{fbL} + b_{fbR} + t_w)(b_{fbR} - b_{fbL})t_{fb}}{2A}$
	y_G^*	$\frac{(h - t_{ft} - t_{fb})(t_{ft} - t_{fb})t_w - (b_{flL} + b_{flR} + t_w)(h - t_{ft})t_{ft} + (b_{fbL} + b_{fbR} + t_w)(h - t_{fb})t_{fb}}{2A}$
	h_t	$\frac{h - t_{ft}}{2} + y_G$
	h_b	$\frac{h - t_{fb}}{2} - y_G$
	\bar{I}_x	$\frac{1}{12}[(h - t_{ft} - t_{fb})^3 t_w + (b_{flL} + b_{flR} + t_w)t_{ft}^3 + (b_{fbL} + b_{fbR} + t_w)t_{fb}^3]$ $+ \left(\frac{t_{ft} - t_{fb}}{2} - y_G\right)^2 (h - t_{ft} - t_{fb})t_w + \left(\frac{h - t_{ft}}{2} + y_G\right)^2 (b_{flL} + b_{flR} + t_w)t_{ft}$ $+ \left(\frac{h - t_{fb}}{2} - y_G\right)^2 (b_{fbL} + b_{fbR} + t_w)t_{fb}$
	I_x^*	$\bar{I}_x + Ay_G^2$
	\bar{I}_y	$\frac{1}{12}[(h - t_{ft} - t_{fb})t_w^3 + (b_{flL} + b_{flR} + t_w)^3 t_{ft} + (b_{fbL} + b_{fbR} + t_w)^3 t_{fb}]$ $+ (x_G)^2 (h - t_{ft} - t_{fb})t_w + \left(\frac{b_{flR} - b_{flL}}{2} - x_G\right)^2 (b_{flL} + b_{flR} + t_w)t_{ft}$ $+ \left(\frac{b_{fbR} - b_{fbL}}{2} - x_G\right)^2 (b_{fbL} + b_{fbR} + t_w)t_{fb}$
	I_y^*	$\bar{I}_y + Ax_G^2$
	J	$\frac{1}{3}[(h - t_{ft} - t_{fb})t_w^3 + (b_{flL} + b_{flR} + t_w)t_{ft}^3 + (b_{fbL} + b_{fbR} + t_w)t_{fb}^3]$
	β_x	$\frac{2\bar{I}_x}{R_y}$
	β_y	$\frac{2\bar{I}_y}{R_y}$
	R_y	$(b_{fbR} + b_{fbL} + t_w)(h - t_{fb})t_{fb} - (b_{flR} + b_{flL} + t_w)(h - t_{ft})t_{ft} + (h - t_{ft} - t_{fb})(t_{ft} - t_{fb})t_w$ $+ \frac{A[h_t b_{flR}(h - t_{ft})t_{ft} + h_t b_{flL}(h - t_{ft})t_{ft} + h_b b_{fbR}(h - t_{fb})t_{fb} + h_b b_{fbL}(h - t_{fb})t_{fb}]}{h_t b_{flR} t_{ft} + h_t b_{flL} t_{ft} - h_b b_{fbR} t_{fb} - h_b b_{fbL} t_{fb}}$
	γ_t	$\alpha_x b_t$
	α_y	$\frac{3A\beta_y}{2(h_t b_{flR} t_{ft} + h_t b_{flL} t_{ft} - h_b b_{fbR} t_{fb} - h_b b_{fbL} t_{fb})}$
	I_{wb}	$\beta_x^2 A + \frac{\alpha_x^2 b_t^2 t_w (h - t_{ft} - t_{fb})^5}{30\left(\frac{h}{2} - t_{fb}\right)^2 \left(\frac{h}{2} - t_{ft}\right)^2} - \frac{\alpha_x \beta_x b_t t_w (h - t_{ft} - t_{fb})^3}{3\left(\frac{h}{2} - t_{fb}\right)\left(\frac{h}{2} - t_{ft}\right)} - \bar{I}_y$
I_{wc}	$B_y^2 A + \frac{8}{15}\alpha_y^2 (h_t^2 b_{flR} t_{ft} + h_t^2 b_{flL} t_{ft} + h_b^2 b_{fbR} t_{fb} + h_b^2 b_{fbL} t_{fb})$ $- \frac{4}{3}\alpha_y \beta_y (h_t b_{flR} t_{ft} + h_t b_{flL} t_{ft} - h_b b_{fbR} t_{fb} - h_b b_{fbL} t_{fb}) - \bar{I}_x$	
I_{cb}	$\frac{\alpha_x^2 b_t^2 t_w (h - t_{ft} - t_{fb})^3}{3\left(\frac{h}{2} - t_{fb}\right)^2 \left(\frac{h}{2} - t_{ft}\right)^2}$	
I_{ec}	$\frac{4}{3}\alpha_y^2 \left(\frac{h_t^2 t_{ft}}{b_{flR}} + \frac{h_t^2 t_{ft}}{b_{flL}} + \frac{h_b^2 t_{fb}}{b_{fbR}} + \frac{h_b^2 t_{fb}}{b_{fbL}}\right)$	

*In (\hat{x}, \hat{y}) coordinate system

Table 5 Coefficients of T-shaped sections

Section	Parameter	Expression
T-section	A	$2bt_f + ht_w$
	$x_G(b_t)$	0
	y_G	$-bt_f(h - t_f)/(2bt_f + ht_w)$
	h_t	$ht_w(h - t_f)/(4bt_f + 2ht_w)$
	h_b	$(t_w h^2 + 4bht_f - 2bt_f^2)/(4bt_f + 2ht_w)$
	\bar{I}_x	$(4b^2t_f^4 + 8bh^3t_ft_w - 12bh^2t_f^2t_w + 8bht_f^3t_w + h^4t_w^2)/(24bt_f + 12ht_w)$
	\bar{I}_y	$(t_f(2b + t_w)^3)/12 + (t_w^3(h - t_f))/12$
	J	$(t_f^3(2b + t_w))/3 + (t_w^3(h - t_f))/3$
	β_x	0
	β_y	$(4b^2t_f^4 + 8bh^3t_ft_w - 12bh^2t_f^2t_w + 8bht_f^3t_w + h^4t_w^2)/(6ht_w(h - t_f)(2bt_f + ht_w))$
	γ_t	0
	α_y	$((4bt_f + 2ht_w)(6bt_f + 3ht_w)(4b^2t_f^4 + 8bh^3t_ft_w - 12bh^2t_f^2t_w + 8bht_f^3t_w + h^4t_w^2)) / (4bh^2t_ft_w^2(h - t_f)^2(12bt_f + 6ht_w))$
	I_{wb}	$(t_f(2b + t_w)^3)/12 + (t_w^3(h - t_f))/12$
	I_{wc}	$(8b^4t_f^8 + 32b^3h^3t_f^5t_w - 48b^3h^2t_f^6t_w + 52b^3ht_f^7t_w + 32b^2h^6t_f^2t_w^2 - 96b^2h^5t_f^3t_w^2 + 190b^2h^4t_f^4t_w^2 - 156b^2h^3t_f^5t_w^2 + 72b^2h^2t_f^6t_w^2 + 28bh^7t_ft_w^3 - 42bh^6t_f^2t_w^3 + 33bh^5t_f^3t_w^3 + 3h^8t_w^4) / (180bh^2t_ft_w^2(h - t_f)^2)$
	I_{eb}	0
	I_{ec}	$8\alpha_y^2h^2t_f/3b$
	\hat{x}_c	0
	\hat{y}_c	$-(h - t_f)/2$
	C_w	$(2b - t_w)^3t_f^3/144 + (h - \frac{t_f}{2})^3t_w^3/36$

Table 6 Coefficients of U-shaped sections

Section	Parameter	Expression
U-section	A	$2bt_f + ht_w$
	$x_G(b_t)$	$bt_f(b + t_w)/(2bt_f + ht_w)$
	y_G	0
	h_t	$(h - t_f)/2$
	h_b	$(h - t_f)/2$
	\bar{I}_x	$t_w h^3/12 + bh^2 t_f/2 - bht_f^2 + 2bt_f^3/3$
	\bar{I}_y	$(4b^4 t_f^2 + 8b^3 ht_f t_w + 12b^2 ht_f t_w^2 + 8bht_f t_w^3 + h^2 t_w^4)/(12(2bt_f + ht_w))$
	J	$2t_f^3(b + t_w)/3 + t_w^3(b - 2t_f)/3$
	β_x	$(4b^4 t_f^2 + 8b^3 ht_f t_w + 12b^2 ht_f t_w^2 + 8bht_f t_w^3 + h^2 t_w^4)/(12bt_f(b + t_w)(2bt_f + ht_w))$
	β_y	0
	γ_t	$(4b^4 t_f^2 + 8b^3 ht_f t_w + 12b^2 ht_f t_w^2 + 8bht_f t_w^3 + h^2 t_w^4)/(8bt_f t_w(b + t_w)(h - 2t_f))$
	α_y	$3\bar{I}_x/(b(h - t_f)^2 t_f)$
	I_{wb}	$(96b^8 t_f^4 + 224b^7 ht_f^3 t_w + 320b^7 t_f^4 t_w + 64b^6 h^2 t_f^2 t_w^2 + 976b^6 ht_f^3 t_w^2 + 480b^6 t_f^4 t_w^2 + 192b^5 h^2 t_f^2 t_w^3 + 2184b^5 ht_f^3 t_w^3 + 240b^5 t_f^4 t_w^3 + 380b^4 h^2 t_f^2 t_w^4 + 2600b^4 ht_f^3 t_w^4 + 16b^3 h^3 t_f t_w^5 + 472b^3 h^2 t_f^2 t_w^5 + 1680b^3 ht_f^3 t_w^5 + 24b^2 h^3 t_f t_w^6 + 384b^2 h^2 t_f^2 t_w^6 + 480b^2 ht_f^3 t_w^6 + 26bh^3 t_f t_w^7 + 140bh^2 t_f^2 t_w^7 + h^4 t_w^8 + 10h^3 t_f t_w^8)/(720b^2 t_f^2 t_w(b + t_w)^2(h - 2t_f))$
	I_{wc}	$2\alpha_y^2(h - t_f)^2 bt_f/15$
	I_{eb}	$(4b^4 t_f^2 + 8b^3 ht_f t_w + 12b^2 ht_f t_w^2 + 8bht_f t_w^3 + h^2 t_w^4)^2/(12b^2 t_f^2 t_w(b + t_w)^2(h - 2t_f)^3)$
	I_{ec}	$2\alpha_y^2(h - t_f)^2 t_f/(3b)$
	\hat{x}_c	$-3(b + t_w/2)^2 t_f/(3(2b + t_w)t_f + (h - t_f)t_w)$
	\hat{y}_c	0
	C_w	$(h - t_f)^2(b + t_w/2)^3 t_f[(1 - 3/(2 + (h - t_f)t_w/(3(b + t_w/2)t_f)))/6 + 1/(8 + 4(h - t_f)t_w/(3(b + t_w/2)t_f))]$

Table 7 Coefficients of L-shaped sections

Section	Parameter	Expression
L-section	A	$bt_f + ht_w$
	$x_G(b_t)$	$bt_f(b + t_w)/(2bt_f + 2ht_w)$
	y_G	$bt_f(h - t_f)/(2bt_f + 2ht_w)$
	h_t	$(t_w h^2 + 2bht_f - bt_f^2)/(2bt_f + 2ht_w)$
	h_b	$ht_w(h - t_f)/(2bt_f + 2ht_w)$
	\bar{I}_x	$(b^4 t_f^4 + 4bh^3 t_f t_w - 6bh^2 t_f^2 t_w + 4bht_f^3 t_w + h^4 t_w^2)/(12bt_f + 12ht_w)$
	\bar{I}_y	$(b^4 t_f^4 + 4b^3 ht_f t_w + 6b^2 ht_f^2 t_w + 4bht_f^3 t_w + h^2 t_w^4)/(12bt_f + 12ht_w)$
	J	$t_f^3(b + t_w)/3 + (t_w^3(h - t_f))/3$
	β_x	$(b^4 t_f^2 + 4b^3 ht_f t_w + 6b^2 ht_f^2 t_w + 4bht_f^3 t_w + h^2 t_w^4)/(6bt_f(b + t_w)(bt_f + ht_w))$
	β_y	$(b^2 t_f^4 + 4bh^3 t_f t_w - 6bh^2 t_f^2 t_w + 4bht_f^3 t_w + h^4 t_w^2)/(6ht_w(h - t_f)(bt_f + ht_w))$
	γ_t	$(h(h/2 - t_f)(b^4 t_f^2 + 4b^3 ht_f t_w + 6b^2 ht_f^2 t_w + 4bht_f^3 t_w + h^2 t_w^4))/(2bt_f t_w(b + t_w)(h - t_f)^3)$
	α_y	$((2bt_f + 2ht_w)(3bt_f + 3ht_w)(b^2 t_f^4 + 4bh^3 t_f t_w - 6bh^2 t_f^2 t_w + 4bht_f^3 t_w + h^4 t_w^2)) / (2bh^2 t_f t_w^2 (h - t_f)(6bt_f + 6ht_w))$
	I_{wb}	$(6b^8 t_f^4 + 28b^7 ht_f^3 t_w + 20b^7 t_f^4 t_w + 16b^6 h^2 t_f^2 t_w^2 + 122b^6 ht_f^3 t_w^2 + 30b^6 t_f^4 t_w^2 + 48b^5 h^2 t_f^2 t_w^3 + 273b^5 ht_f^3 t_w^3 + 15b^5 t_f^4 t_w^3 + 95b^4 h^2 t_f^2 t_w^4 + 325b^4 ht_f^3 t_w^4 + 8b^3 h^3 t_f t_w^5 + 118b^3 h^2 t_f^2 t_w^5 + 210b^3 ht_f^3 t_w^5 + 12b^2 h^3 t_f t_w^6 + 96b^2 h^2 t_f^2 t_w^6 + 60b^2 ht_f^3 t_w^6 + 13bh^3 t_f t_w^7 + 35bh^2 t_f^2 t_w^7 + h^4 t_w^8 + 5h^3 t_f t_w^8)/(180b^2 t_f^2 t_w(b + t_w)^2(h - t_f))$
	I_{wc}	$(b^4 t_f^8 + 8b^3 h^3 t_f^5 t_w - 12b^3 h^2 t_f^6 t_w + 13b^3 ht_f^7 t_w + 16b^2 h^6 t_f^2 t_w^2 - 48b^2 h^5 t_f^3 t_w^2 + 95b^2 h^4 t_f^4 t_w^2 - 78b^2 h^3 t_f^5 t_w^2 + 36b^2 h^2 t_f^6 t_w^2 + 28bh^7 t_f t_w^3 - 42bh^6 t_f^2 t_w^3 + 33bh^5 t_f^3 t_w^3 + 6h^8 t_w^4)/(180bh^2 t_f t_w^2 (h - t_f)^2)$
	I_{eb}	$(b^4 t_f^2 + 4b^3 ht_f t_w + 6b^2 ht_f^2 t_w + 4bht_f^3 t_w + h^2 t_w^4)/(3b^2 t_f^2 t_w(b + t_w)^2(h - t_f)^3)$
	I_{ec}	$4\alpha_y^2 h_b^2 t_f/3b$
	\hat{x}_c	0
\hat{y}_c	$(h - t_f)/2$	
C_w	$[(h - t_f/2)^3 t_w^3 + (b + t_w/2)^3 t_f^3]/36$	

Acknowledgements The authors highly appreciate the supports provided by the Center of Excellence in Composite Structures and Seismic Strengthening (CECSSS) at Sharif University of Technology (SUT).

Data availability Data supporting this study are included within the article and supporting materials.

Declarations

Conflict of interest The authors declare that there is no conflict of interests regarding the publication of this paper.

Ethical approval This material is the authors' own original work, which has not been previously published elsewhere. The paper is not currently being considered for publication elsewhere. The paper reflects the authors' own research and analysis in a truthful and complete manner. The paper properly credits the meaningful contributions of co-authors and co-researchers. All authors have been personally and actively involved in substantial work leading to the paper, and will take public responsibility for its content. I agree with the above statements and declare that this submission follows the policies of journal as outlined in the Guide for Authors and in the Ethical Statement.

References

1. Kwan AKH. Shear lag in shear/core walls. *J Struct Eng.* 1996;122:1097–104.
2. Hoult RD. Shear lag effects in reinforced concrete C-shaped walls. *J Struct Eng.* 2019;145:4018270.
3. Fahmy EH, Robinson H. Analyses and tests to determine the effective widths of composite beams in unbraced multistorey frames. *Can J Civ Eng.* 1986;13:66–75.
4. Cambronero-Barrientos F, Díaz-del-Valle J, Martínez-Martínez J-A. Beam element for thin-walled beams with torsion, distortion, and shear lag. *Eng Struct.* 2017;143:571–88.
5. Li X, Wan S, Mo YL, Shen K, Zhou T, Nian Y. An improved method for analyzing shear lag in thin-walled box-section beam with arbitrary width of cantilever flange. *Thin Walled Struct.* 2019;140:222–35.
6. Argyridi AK, Sapountzakis EJ. Advanced analysis of arbitrarily shaped axially loaded beams including axial warping and distortion. *Thin Walled Struct.* 2019;134:127–47.
7. Lezgy-Nazargah M, Vidal P, Polit O. A sinus shear deformation model for static analysis of composite steel-concrete beams and

- twin-girder decks including shear lag and interfacial slip effects. *Thin Walled Struct.* 2019;134:61–70.
8. Luo D, Zhang Z, Li B. The effects of shear deformation in non-rectangular steel reinforced concrete structural walls. *J Constr Steel Res.* 2020;169: 106043.
 9. Zhou M, Zhang Y, Lin P, Zhang Z. A new practical method for the flexural analysis of thin-walled symmetric cross-section box girders considering shear effect. *Thin Walled Struct.* 2022;171: 108710.
 10. Palermo D, Vecchio FJ, Solanki H. Behavior of three-dimensional reinforced concrete shear walls. *ACI Struct J.* 2002;99:81–9.
 11. Thomsen JH IV, Wallace JW. Displacement-based design of slender reinforced concrete structural walls—experimental verification. *J Struct Eng.* 2004;130:618–30.
 12. Zhang Z, Li B. Seismic performance assessment of slender T-shaped reinforced concrete walls. *J Earthq Eng.* 2016;20:1342–69.
 13. Constantin R, Beyer K. Behaviour of U-shaped RC walls under quasi-static cyclic diagonal loading. *Eng Struct.* 2016;106:36–52.
 14. Brueggen BL, French CE, Sritharan S. T-shaped RC structural walls subjected to multidirectional loading: test results and design recommendations. *J Struct Eng.* 2017;143:4017040.
 15. Ma J, Zhang Z, Li B. Experimental assessment of T-shaped reinforced concrete squat walls. *ACI Struct J.* 2018;115:621–34.
 16. Hoult R, Beyer K. RC U-shaped walls subjected to in-plane, diagonal, and torsional loading: new experimental findings. *Eng Struct.* 2021;233: 111873.
 17. Palermo D, Abdulridha A, Charette M. Flange participation for seismic design of reinforced concrete shear walls. 2007. p. 1210–19
 18. Zhang Z, Luo D, Li B. Strain nonlinearity and shear lag effect in compressive flange of reinforced concrete structural walls. *ACI Struct J.* 2021;118.
 19. Khaloo A, Tabiee M, Abdoos H. A numerical laboratory for simulation of flanged reinforced concrete shear walls. *J Numer Methods Civ Eng.* 2022;6:92–102.
 20. Reissner E. Analysis of shear lag in box beams by the principle of minimum potential energy. *Q Appl Math.* 1946;4:268–78.
 21. Song Q, Scordelis AC. Shear-lag analysis of T-, I-, and box beams. *J Struct Eng.* 1990;116:1290–305.
 22. Haji-Kazemi H, Company M. Exact method of analysis of shear lag in framed tube structures. *Struct Des Tall Build.* 2002;11:375–88.
 23. *Building Code Requirements for Structural Concrete (ACI 318-19).* 2020.
 24. *Iranian Concrete Code of Practice (ABA). Planning and management organization, PN, 120.* 2021.
 25. E. CEN. 8—Design of structures for earthquake resistance—Part 1: general rules, seismic actions and rules for building. London: Br. Stand. Institute; 2004.
 26. *Uniform Building Code, 1994, International Code Council; 1994.*
 27. B.S. BS5400, Steel, concrete and composite bridges, Part 5, code of practice for design of composite bridges. London: Br. Stand. Institution; 1979.
 28. Brueggen BL. Performance of T-shaped reinforced concrete structural walls under multi-directional loading. Ph.D. Dissertation. 2009.
 29. Choi C-S, Ha S-S, Lee L-H, Oh Y-H, Yun H-D. Evaluation of deformation capacity for RC T-shaped cantilever walls. *J Earthq Eng.* 2004;8:397–414.
 30. Beyer K, Dazio A, Priestley MJN. Quasi-static cyclic tests of two U-shaped reinforced concrete walls. *J Earthq Eng.* 2008;12:1023–53.
 31. Zhang Z, Li B. Shear lag effect in tension flange of RC walls with flanged sections. *Eng Struct.* 2017;143:64–76.
 32. Shi Q, Wang B. Simplified calculation of effective flange width for shear walls with flange. *Struct Des Tall Spec Build.* 2016;25:558–77.
 33. Liu C, Wei X, Wu H, Li Q, Ni X. Research on shear lag effect of t-shaped short-leg shear wall. *Period Polytech Civ Eng.* 2017;61:602–10.
 34. Ni X, Cao S. Shear lag analysis of I-shaped structural members. *Struct Des Tall Spec Build.* 2018;27: e1471.
 35. Lu N, Li W. Analytical study on the effective flange width for T-shaped shear walls. *Period Polytech Civ Eng.* 2020;64:253–64.
 36. Tabiee M, Abdoos H, Khaloo A. Investigation of the shear-lag effects on the response of L-shaped RC shear walls. *J Struct Constr Eng.* 2022. <https://doi.org/10.22065/jsce.2022.340500.2804>.
 37. Abdoos H, Khaloo A, Tabiee M. Effective width estimation of L-shaped RC shear walls using EPR algorithm. *Sharif J Civ Eng.* 2023;38(2):63–71.
 38. Lue DM, Liu J-L, Lin C-H. Numerical evaluation on warping constants of general cold-formed steel open sections. *Steel Struct.* 2007;7:297–309.
 39. Carpinteri A, Lacidogna G, Nitti G. Open and closed shear-walls in high-rise structural systems: static and dynamic analysis. *Curved Layer Struct.* 2016;3(1):154–71.
 40. Capdevielle S, Grange S, Dufour F, Desprez C. A multifiber beam model coupling torsional warping and damage for reinforced concrete structures. *Eur J Environ Civ Eng.* 2016;20:914–35.
 41. Di Re P, Addessi D, Filippou FC. Mixed 3D beam element with damage plasticity for the analysis of RC members under warping torsion. *J Struct Eng.* 2018;144:4018064.
 42. R. Constantin, K. Beyer. Non-rectangular RC walls: a review of experimental investigations. In: 2nd European conference earthquake engineering seismology, 2014
 43. Khaloo H, Tabiee AR, Abdoos M. Analytical study of distribution of shear lag-induced stress in non-rectangular reinforced concrete shear walls. In: 12th international congress on civil engineering, 2021. p. 8.
 44. Lezgy-Nazargah M, Vidal P, Polit O. A quasi-3D finite element model for the analysis of thin-walled beams under axial–flexural–torsional loads. *Thin Walled Struct.* 2021;164: 107811.
 45. Khaloo H, Tabiee AR, Abdoos M. Analytical study of distribution of shear lag-induced stress in non-rectangular reinforced concrete shear walls. In: 12th international congress on civil engineering, Mashhad, Iran [In Persian], 2021. p. 8.
 46. Tabiee M. Study of shear lag effect on non-rectangular RC shear walls, M.Sc. Thesis, Sharif University of Technology, 2021.
 47. Martin H. Elasticity-theory, applications, and numerics. Elsevier Science Publishing Company; 2014.
 48. Vlasov VZ. Thin-walled elastic rods. Moscow: Fizmatgiz; 1959.
 49. Bleich F. Buckling strength of metal structures. Cardnr: Mc Graw-Hill B. Company Inc; 1952. p. 51–12588.
 50. I. canadien de la construction en acier, D. Beaulieu, Calcul des charpentiers d'acier, [Willowdale, Ont.]: Institut canadien de la construction en acier, 2003.
 51. Galambos TV. Structural members and frames. Upper Saddle River: Prentice-Hall; 1968.
 52. Seaburg PA, Carter CJ. Torsional analysis of structural steel members, 1997.
 53. Galambos TV. Guide to stability design criteria for metal structures. New York: Wiley; 1998.
 54. Bryan SS, Alex C. Tall building structures: analysis and design (1991)
 55. Ma J, Li B. Experimental and analytical studies on H-shaped reinforced concrete squat walls. *ACI Struct J.* 2018;115:425–38.
 56. Behrouzi AA, Mock AW, Lehman DE, Lowes LN, Kuchma DA. Impact of bi-directional loading on the seismic performance of C-shaped piers of core walls. *Eng Struct.* 2020;225: 111289.

57. Roy HEH, Sozen MA. Ductility of concrete. Spec Publ. 1965;12:213–35.
58. Park R, Paulay T. Reinforced concrete structures. New York: Wiley; 1975.

Publisher's Note Springer Nature remains neutral with regard to jurisdictional claims in published maps and institutional affiliations.

Springer Nature or its licensor (e.g. a society or other partner) holds exclusive rights to this article under a publishing agreement with the author(s) or other rightsholder(s); author self-archiving of the accepted manuscript version of this article is solely governed by the terms of such publishing agreement and applicable law.